Définition du style : TM 1

Deliverable 7.4: HITEC - Specific GAS/HITEC technical report on self-sealing processes

Work Package 7

The project leading to this application has received funding from the European Union's Horizon 2020 research and innovation programme under grant agreement No 847593.

http://www.ejp-eurad.eu/

Document information

Project Acronym	**EURAD**
Project Title	**European Joint Programme on Radioactive Waste Management**
Project Type	**European Joint Programme (EJP)**
EC grant agreement No.	**847593**
Project starting / end date	**1 June 2019 – 31 May 2024**
Work Package No.	**7**
Work Package Title	**Influence of Temperature on Clay-based Material Behaviour**
Work Package Acronym	**HITEC**
Deliverable No.	**7.4**
Deliverable Title	**Specific GAS/HITEC technical report on self-sealing processes**
Lead Beneficiary	**[Andra]**
Contractual Delivery Date	**May 2024**
Actual Delivery Date	**June 2024**
Type	**Report**
Dissemination level	**PU**
Authors	**Jean Talandier (Andra), Christophe de Lesquen (Andra), Dragan Grgic (CNRS-ULorraine), Dewinde Agboli (CNRS-ULorraine), Pierre Bésuelle (CNRS-UGrenoble), Rob Cuss (UKRI-BGS), Andrew Wiseall (UKRI-BGS), Frédéric Colin (ULiège), Marketa Kucerova (CTU), Laura Gonzalez-Blanco (CIMNE), Enrique Romero (CIMNE), Quasim Llabjan (EPFL), Alessio Ferrari (EPFL), Chun-Liang Zhang (GRS)**

To be cited as:

Talandier J., de Lesquen C., Grgic, D., Agboli D., Bésuelle, P., Cuss R., Wiseall A., Colin F., Kucerova M., Gonzalez-Blanco L., Romero E., Llabjani Q., Ferrari A., Zhang C.-L. (2024). Specific GAS/HITEC technical report on self-sealing processes. Final version as of 31.05.2024 of deliverable D7.4 of the HORIZON 2020 project EURAD. EC Grant agreement no: 847593.

Disclaimer

Acknowledgement

This document is a deliverable of the European Joint Programme on Radioactive Waste Management (EURAD). EURAD has received funding from the European Union's Horizon 2020 research and innovation programme under grant agreement No 847593.

Status of deliverable		
	By	Date
Delivered (Lead Beneficiary)	[Andra].	28 May 2024
Verified (WP Leader)	Markus Olin [VTT]	28 May 2014
Reviewed (Reviewers)	N. Conil	31 May 2024
Approved (PMO)	Bharti Reddy	04/06/2024
Submitted to EC	Andra (Coordinator)	05/06/2024

Executive Summary

In underground waste repositories, the host rock is submitted to a number of successive solicitations induced by the excavation and then by the emplacement of the waste. The excavation creates a damaged zone around the structures, while the wastes, particularly high-level waste materials, will lead to an increase in temperature. After closure, water coming from the host rock starts to saturate all the materials including the damaged zone. Corrosion of metallic components will lead to an increase of gas pressure in the repository. Self-sealing occurs in the fractures of the damaged zone at the early stages when water is coming back from the clay layer. Depending on the position in the repository, during this resaturation, temperature can increase in the fractured zone. In general, gas pressure will increase later when the damaged zone is resaturated and temperature has decreased. The same kind of exposure to high temperature and gas solicitations happens for the clay barriers.

Similar self-sealing experiments were performed by HITEC WP subtask 2.1 (influence of temperature) and GAS WP subtask 3.2 (influence of gas pressure). In WP HITEC, the interactions between self-sealing and temperature was explored. In WP GAS, self-sealed materials were exposed to gas to observe potential modifications of the self-sealing capacity of the clay materials. Logically, questions may arise concerning the self-sealing of fractures subjected successively to high temperature and then to gas pressure. The collaborative actions between the HITEC WP and the GAS WP aimed to address these situations through a dedicated experimental programme carried out by teams involved in both WPs on the issue of self-sealing. Because of time constraints due to the Covid, these experiments could unfortunately not be completed. This final report presents the laboratory tests performed in the GAS and HITEC work packages, their results, our understanding of the self-sealing process, the similarities and differences between the different claystones and the effectiveness of the self-sealing process under temperature and gas.

Table of content

List of figures

List of Tables

1. Introduction

Clay formations are being considered as a suitable host rock for the deep geological disposal of radioactive waste in Belgium, France and Switzerland. In addition to their favourable properties such as low permeability and high sorption capacity for radionuclides, these rocks have an interesting "self-sealing" capacity (Bock et al, 2010): fractures generated in argillaceous formations have the capacity to become less hydraulically conductive with time when exposed to water.

In underground waste repositories, the host rock is subjected to a number of successive solicitations induced by the excavation and then by the emplacement of the waste packages. This is illustrated on Figure 1-1 by some results of thermo-hydraulic simulations in the near-field of a SF/HLW repository (Senger et al, 2014). The excavation creates a damaged zone around the structures, while the wastes, particularly high-level waste materials, will lead to an increase in temperature (Figure 1-1, upper right). After closure, water coming from the host rock starts to saturate all the materials including the damaged zone, and the self-sealing process of the induced fractures can begin. At the same time, the corrosion of metallic components will generate large volumes of gas leading to a pressure build-up in the repository (Figure 1-1, upper left). Depending on the position in the repository, during this resaturation, the temperature can increase in the fractured zone. However, in general, the gas pressure increases later when the damaged zone is resaturated and temperature is decreasing (Figure 1-1, upper right and left).

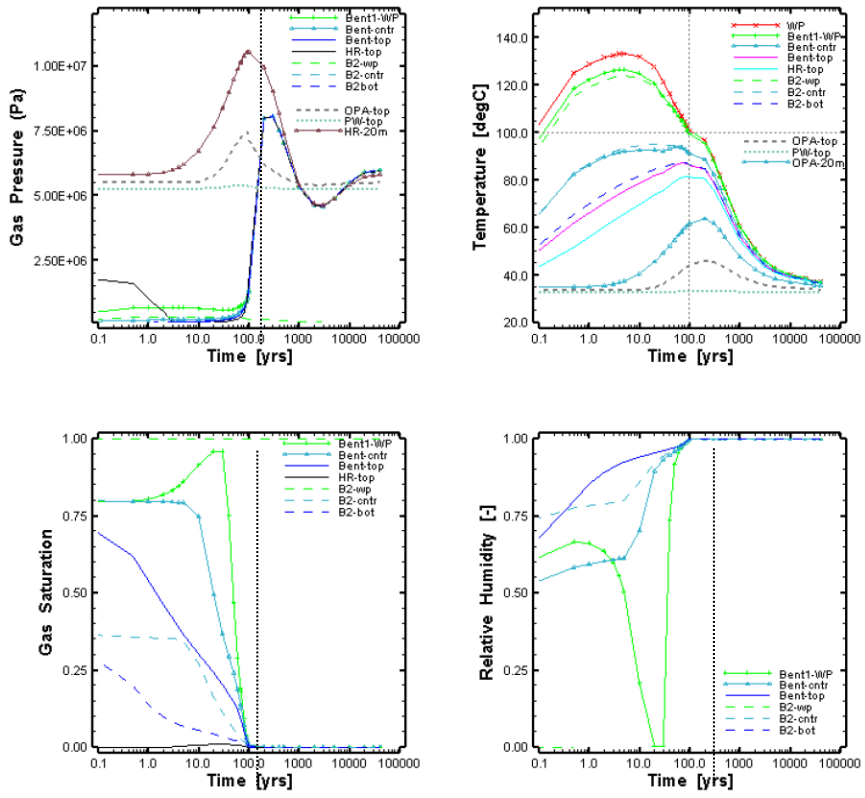

Figure 1-1 – 3D model results of resaturation and heating for repository in Opalinus Clay: Time history at different locations in the bentonite buffer and surrounding host rock of gas pressure (upper left),

temperatures (upper right), gas saturation (lower left), and computed relative humidity (lower right), (Senger et al. 2014)

The bentonite used as buffer material will experience similar temperature and gas solicitations.

In WP HITEC, the interactions between self-sealing and temperature were explored. In WP GAS, two situations have been explored:

- Self-sealed materials were exposed to gas to observe potential modifications of the self-sealing capacity of the clay materials.
- Hydromechanical properties of clay materials were characterised before and after gas breakthrough test.

Logically, questions may arise concerning the self-sealing of fractures subjected successively to high temperature and then to gas pressure. The collaborative actions between the HITEC WP and the GAS WP aimed to address these situations through a dedicated experimental programme carried out by teams involved in both WPs on the issue of self-sealing. Because of time constraints due to the Covid, these experiments could unfortunately not be completed.

2. HITEC and GAS laboratory experiments

Several partners performed tests in HITEC and GAS concerning self-sealing behaviour of clay host rocks and bentonite materials used as buffer materials.

Among these partners, three of them were involved in both the HITEC and GAS work packages: BGS, CTU and ULorraine. These teams initially planned to perform sequentially thermal and gas tests on the same sample, with the objective to compare these tests with the tests with temperature or gas only. However, because of the delays due to Covid, these specific tests could not be carried out. A short description of the tests performed in each WP will therefore be presented here.

Other partners were involved only in HITEC such as UGrenoble, or in GAS such as GRS, UPC, EPFL.

Reference is made to the HITEC D7.3 and GAS D6.8 deliverables for more details on the experiments.

2.1 Self-sealing in clay materials

Self-sealing depends on thermo- hydro-mechanical and chemical processes, the mineral composition of the material in link with its swelling capacity and controlled by the prevailing state conditions. Mechanical closure of fractures, hydro-chemical interactions of the pore water with the clay-bearing solid phase of the geomaterial (e.g., swelling, dis-aggregation) and colloidal transport processes (e.g. sedimentation, clogging) have been identified as typical self-sealing mechanisms in clay-rich materials. Self-sealing mechanisms are well identified for host rock (Boom Clay, Opalinus Clay and Callovo-Oxfordian claystone) and bentonite-based materials used for engineered barriers.

Although a basic understanding and identification of the phenomena and processes that contribute to self-sealing has been achieved, a certain amount of knowledge still needs to be consolidated on the consequences for self-sealing in clay materials when these are subjected to gas pressure or high temperature.

An improvement of conceptualization of self-sealing mechanisms at process level is needed to be able to model and predict the self-sealing capacity of clay barriers and the host rocks under the THM-C conditions that prevail in a deep geological repository.

Several situations have to be explored to demonstrate that self-sealing capacity is not lost due to gas breakthrough or thermal effect such as:

- successive opening/closing of gas pathways in particular for engineered barriers or at the interfaces between clay materials and other components of the repository.

- long-term gas flow in a fracture and possible transformations or microstructural reorganisations at the fracture wall
- impact of heating on the self-sealing processes in the near field.

2.1.1 Self-sealing in bentonite-based buffer materials

The exposure of the engineered-barrier system to high gas pressures may induce the development of dilatant pathway or even fracturing. Once the gas pressure decreases and the buffer is resaturated, it is important to check that the sealing capacity of the clay barrier is re-established.

One laboratory experiment was conducted in GAS Task 3:

- **CTU – Cyclical water and gas injection experiments with Czech Ca-Mg bentonite.** The experimental process included multiple cycles of sample (re)saturation, hydraulic conductivity measurement, and gas breakthrough testing using constant volume cells. After the testing was completed, the cells were dismantled and various sample characteristics, such as water content, density, and dry density, were determined. The tests were performed on BCV bentonite (Ca-Mg type).

2.1.2 Self-sealing in clay host rocks

When subjected to excessive gas pressures, intact clayey rocks are particularly prone to failure due to their low mechanical strength. The consequences of the dilatant pathway formation or gas fracturing on the properties such as water permeability is of major concern for the long-term safety of the repository.

Gas pressure and temperature increasing concern first the damaged zone created during the excavation of the tunnel. There is some evidence that this zone will self-seal due to resaturation.

Three geomaterials were investigated in the GAS and HITEC WP, namely Boom Clay (BC), a normally consolidated stiff soil, Callovo Oxfordian (Cox), a normally consolidated soft rock and Opalinus Clay, a moderately overconsolidated soft rock.

Five laboratory experiments were conducted in GAS Task 3 with focus on gas induced failure and self-sealing capacity of clayey host rocks:

- **GRS – Gas transport along fractures in clayey rocks and impact of self-sealing**. The experimental programme consisted of long-term self-sealing and gas injection tests in triaxial cells on artificially fractured claystones (Cox, OPA). Exceptional data bases were acquired by monitoring the evolution of hydraulic conductivity, axial and radial strains over a period of up to 700 days. Gas injection tests on the resealed material were aimed at exploring the gas pressure needed to invade the resealed material under a given confining stress. Resealing tests after completion of gas injection sequences and post-mortem investigations of the dismantled test samples complemented the experimental programme.
- **CNRS (ULorraine) – Visualisation of gas transport in fractures and impact on their self-sealing capacity.** Water and gas permeability tests with flow direction parallel and perpendicular to bedding were conducted in triaxial cells on intact and artificially fractured claystone (Cox). The innovative aspect in the experimental programme was the use of a µ-CT-equipment for the visualization of gas transport processes during gas invasion phase and, subsequently, the self-sealing processes in response to re-hydration of the sample. Evolution of permeability, volumetric strain and fracture volume was monitored in the gas invasion phase and during re-hydration.
- **BGS (UKRI) – Effects of gas transport on fracture transmissivity and self-sealing.** A novel test concept for fracture transmissivity measurements under well-defined shearing conditions was pursued using a highly instrumented (normal stress, shear stress, shear displacement, normal displacement, porewater pressure/flow, etc) bespoke direct shear apparatus. The experiments were conducted with indurated claystones (Cox, OPA). The test results

encompassed not only the transients of gas/water flow, stresses and shear strains but also scans of the fracture surfaces before and after testing. Such complementary spatial information about the evolution of the fracture surface in response to gas injections and re-hydrations provides invaluable insights in the gas transport and self-sealing mechanisms.

- **EPFL – Gas transport in intact and remoulded / recompacted claystone.** Combined water/gas injection experiments were conducted on indurated clay samples (OPA) using a high-pressure oedometric cell, specifically designed for testing at high confining stresses. Special focus was on accurate measurement of the volumetric behaviour of the material during the entire test sequence, comprising the initial sample equilibration phase, water permeability tests, gas injection tests, rehydration tests and a final pressure recovery phase. The experiments were carried out on intact material and on material, which had been remolded and recompacted for mimicking the microfabric of fault gouge material. The impact of gas transport on the microfabric of the test samples was studied as part of a postmortem investigation programme.
- **CIMNE (UPC) – Hydromechanical response of claystones on gas injections.** Combined water/gas injection experiments were conducted with a clayey soft rock (BC). For this, a new oedometric cell was designed and tested, allowing for highly accurate measurements of the volumetric behaviour of the material and for monitoring of the lateral stress acting on the test sample. Outstanding experimental results were achieved with the new cell, indicating a distinct dependence of the gas transport capacity of the BC samples on the gas injection rate. Postmortem studies indicated a measurable impact of the gas injections on the microfabric of the material.

Three laboratory experiments were conducted in HITEC Task 2 with focus on the effect of temperature on the self-sealing:

- **BGS (UKRI) – Self-sealing tests in shear ring.** BGS performed a series of novel experiments using a highly instrumented (normal stress, shear stress, shear displacement, normal displacement, porewater pressure/flow, temperature, etc) bespoke direct shear apparatus, modified to operate at elevated temperatures; the Heated Shear Rig (HSR). The study was planned in Boom Clay, Callovo-Oxfordian (Cox) claystone, and Opalinus Clay. However, at the time of reporting, only Opalinus Clay had been completed, with some tests in Cox claystone. The test results encompassed not only the transients of water flow, stresses and shear strains but also scans of the fracture surfaces before and after testing.
- **UGrenoble (CNRS) – Self-sealing tests in oedometric cell.** The tests of fracture sealing have been performed in an in-house cell that was developed initially for the laboratory x-ray tomograph. The device has been adapted to be used on the D50 beamline from ILL for dual x-ray and neutron tomography and with a temperature control up to 90°C. Cylindrical specimens (centimetric size) were cut from Cox claystone cores and prepared with a synthetic crack in the middle axial plane. Two orientations were considered, parallel and perpendicular to the bedding, The crack was initially open and the specimen placed in oedometric conditions (no radial displacement of the outer boundary). Neutron and x-ray scans were done during the flow of synthetic host pore water (site salinity) through the crack every 15 minutes. Crack closure, local swelling around crack and water re-saturation (water content evolution) were quantified thanks to neutron and x-ray scans and DIC analysis. Tests were performed at three different temperatures (25, 60 and 90°C).
- **ULorraine (CNRS) – Self-sealing tests in triaxial cell.** Self-sealing tests with water injection under different temperatures, calcite contents, sample orientations and initial crack openings were performed on Cox samples. The innovative aspect in the experimental programme was the use of a µ-CT-equipment for the visualization. The particularity of the cell is that its body is made of PEEK CF30 (PolyEtherEtherKetone, 30% carbon fibers) and thus is transparent to X-rays. A confining pressure of 4 MPa was kept constant during the whole tests. 3D X-ray scans were performed on all tested samples before, during and after the experiment and the voxel data were analysed with a high-end software for the visualization and analysis of computed

tomography (CT) data to estimate the evolution of the crack volume. In addition, water permeability was measured continuously during all tests.

2.2 Laboratory tests on bentonite: CTU (Czech Technical University in Prague)

The CTU experimental programme concerned the performance of the bentonite buffer when exposed to processes that may impair the mechanical integrity of the buffer and the study of the consequences of buffer failure. The proposed experiments comprise cyclical water and gas injection experiments using constant volume cells. The tests were performed on BCV bentonite (Ca-Mg type).

In order to address the various research issues, a series of cyclical experimental tests were planned involving the “rapid” injection of gas into samples subjected to a constant volume boundary condition with the intention of attaining a breakthrough event. The 'rapid' buildup of pressure allows observation of the whole spectrum of processes involved in the impact of the initial state (compaction) on the gas transport behaviour and the impact of gas-induced failure on the transport properties; moreover, the cyclical loading approach allows observation of the impact of intermittent gas flow / repeat gas events. A specially designed constant volume cell, which allow for the total saturation of the sample and the subsequent determination of the swelling pressure, was used for testing purposes that involve the injection of the gas medium from the bottom of the sample. The high constant value of the gas pressure allows for the observation of the time required for the occurrence of a breakthrough event and the flow of gas from the sample during/after the breakthrough event via the monitoring of the outflow of gas at the top of the cell. Monitoring total pressure helps monitor the evolution of stress inside the sample. The tested material comprises powdered BCV (Ca-Mg) bentonite compacted to various dry densities (1300-1500 kg/m^3).

2.2.1 Experimental setup

The testing procedure involves the use of specially designed permeameter cells, which comprise a cylindrical steel chamber (ring) for the housing of the samples (diameter: 30 mm, height: 20 mm). The constant volume of the sample is ensured by the rigid structure of the experimental cells while allowing for the monitoring of total pressure. The top and bottom of the samples have been fitted with sintered steel permeable plates to prevent the leaching (“mobilisation”) of the material. The piston and pressure sensor for the measurement of the total (or swelling) pressure of the bentonite is positioned between the upper flange of the chamber and the upper surface of the sample. A pressure sensor is connected to a central data logger. The high-pressure constant volume cell has been designed for the investigation of the flow of both water and gas through the bentonite samples.

The cells are used in two different experimental setups:

- Setup A – the measurement of water permeability and total pressure (Figure 2-1)
- Setup C – the measurement of the “rapid” gas breakthrough tests with total pressure (Figure 2-2)

The gas testing procedure involves the temporary disconnection of the cell from the permeameter (set-up A) and its connection to the gas injection set-up (set-up C).

Czech Ca-Mg bentonite (BCV) was subjected to testing via the uniaxial compaction of the material in the powdered form (initial water content of approximately 10%) in the rings of the cells. Distilled water is used as the saturation medium. The gas used for the breakthrough experiments is compressed dry air.

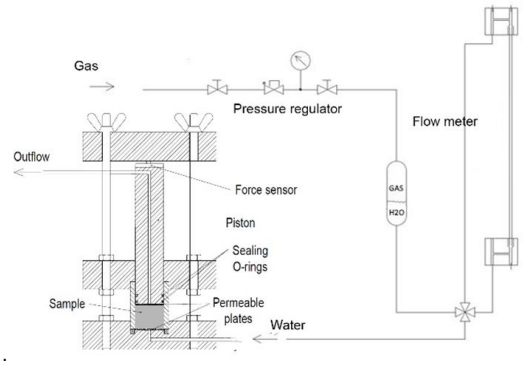

Figure 2-1 – Experimental setup A – water permeability testing and the measurement of total pressure.

Setup A: The apparatus setup as illustrated in Figure 2-1 is used to investigate water permeability and total pressure during the saturation phases. Distilled water is used as the saturation medium, which is pushed into the material using compressed argon. The water flow is determined manually using a graded capillary tube-based flow meter in the inflow part.

The test is conducted up to the point at which the flow and the total pressure are observed to stabilise. The final water flow values are used for the determination of permeability. The water pressure source is subsequently disconnected to allow for the determination of swelling pressure.

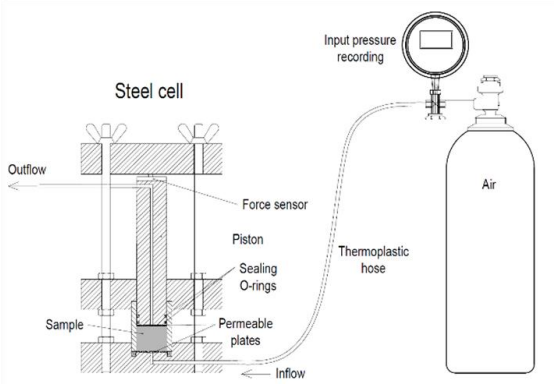

Figure 2-2 – Experimental setup C – "fast" gas breakthrough testing and the measurement of total pressure.

Setup C: The apparatus illustrated in Figure 2-2 is used for the conducting of gas pressure testing. The principle of the test procedure is to subject the sample to a high gas injection pressure until breakthrough occurs. The testing procedure allows for the monitoring of the injection pressure at the inlet to the sample, the total pressure, as measured by pressure sensors positioned on the pistons (i.e. the total pressure that is influenced by the injection pressure) and the gas flow at the outlet of the sample.

Two types of samples were prepared:

- Homogeneous samples: The sample was compacted directly into the cell using a piston (uniaxial compaction) to the desired dry density. Powder material with an initial water content of approximately 10% was used as the sample material.
- Samples with artificial joint (*Figure* 2-3): The sample was compacted into the cell as in the case of a homogeneous sample. Two samples of the same dry density were always compacted and then displaced. Each sample was cut longitudinally by a saw so that a “perfect” half was produced without a cutting through. This 'perfect' half from both samples was used to create one sample with a joint. The two halves were placed into the cell and the cell was connected to the testing apparatus. This specimen preparation procedure was chosen to minimize the loss of material due to cutting.

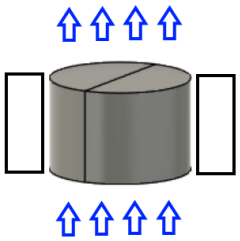

Figure 2-3 – Concept for hydraulic testing / gas testing of joints along bentonite blocks

The experimental procedure comprises two consecutive phases – A (the investigation of saturation, water permeability and swelling pressure) & C (Gas injection). Setup A was used for Phase A (Figure 2-1) and setup C was used for Phase C (Figure 2-2).

Test procedure (one or more cycles):

A) Sample (re)saturation (Set-up A)

i. Compaction of the sample in the cell (ring)
ii. Connection to the permeameter set-up (Figure 2-1, Set-up A)
iii. Saturation, monitoring of water flow and total pressure
iv. Permeability measurement (water)
v. Switching off of the saturation pressure
vi. Swelling pressure measurement

C) Gas injection test (Set-up C)

i. Connection of the cell to the gas injection set-up (Figure 2-2)
ii. Application of a gas injection pressure equal to 12 MPa
iii. Monitoring of the time to the breakthrough event, the injection pressure and the gas flow at the outlet of the sample
iv. Once breakthrough occurs, connection of the cell to the permeameter set-up (Set-up A) and repetition of the testing cycle

The first set of samples contained five homogeneous samples with a dry density ranging from 1290 to 1510 kg/m^3. All samples were placed in the test cells and saturation (Phase A) was initiated. From Phase A, the hydraulic conductivity was determined and the swelling pressure for each sample was estimated.

The second set of samples contained five samples with an artificial longitudinal joint with dry densities ranging from 1318 to 1585 kg/m^3. All samples were placed in the testing cells and saturation (Phase A)

was initiated. From Phase A, the hydraulic conductivity was evaluated and the swelling pressure for each sample was determined. These values were taken as initial values. Table 2-1 provides a summary of the initial state of the samples with artificial joint.

Table 2-1 – Overview of initial state of the samples with an artificial joint

sample no.	ρ_d [kg/m^3]	initial water content [%]	first saturation duration [days]	k [m/s]	σ_{sw} [MPa]	void ratio	porosity	compaction stress [MPa]	initial degree of saturation	degree of saturation after last breakthrough test
P824	1318	12.3	181	8.07E-13	1.72	1.09	0.523	0.5 - 40	0.32	0.66
P846	1360		188	7.56E-13	1.56	1.03	0.507		0.33	0.90
P830	1502		195	2.42E-13	2.20	0.84	0.456		0.41	1.00
P831	1540		190	2.00E-13	4.24	0.79	0.442		0.43	1.02
P832	1585		214	1.35E-13	6.70	0.74	0.426		0.46	1.04

Following the saturation phase, which lasted approximately 6 months for each sample, cyclic loading was initiated. The measuring apparatus was connected to Setup C and a fast gas breakthrough test was performed. During the resaturation phase after the fast gas test, the hydraulic conductivity and the evolution of the swelling pressure were evaluated.

2.2.2 Results

2.2.2.1 Homogeneous samples:

The hydraulic conductivity for all samples was not affected by the fast gas break tests or their frequency. During the test, a moderate long-term decrease was observed. This is most likely a material property.

A summary of the results from all samples is shown in Figure 2-4 and Figure 2-5. Specifically, the change in hydraulic conductivity after gas breakthrough events and resaturation (Figure 2-4) and the change in swelling pressure (Figure 2-5) after fast gas breakthrough tests were monitored.

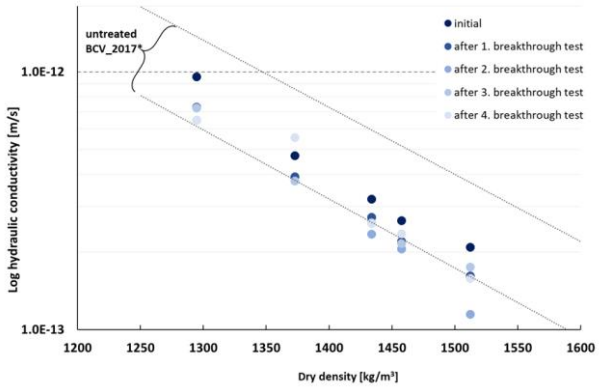

*Figure 2-4 – Hydraulic conductivity (at 10°C) after the fast gas breakthrough tests and resaturation phase for the homogeneous samples of BCV bentonite in comparison with an initial values (*data from Šachlová, 2022).*

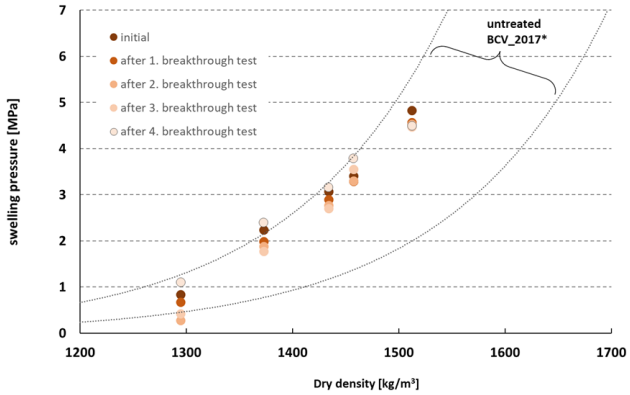

*Figure 2-5 – Swelling pressure after fast gas breakthrough tests and resaturation phase for the homogeneous samples of BCV bentonite (*data from Šachlová, 2022).*

2.2.2.2 Samples with artificial joint:

A summary of the results of all samples with the artificial joint is shown in Figure 2-6 and Figure 2-7. Specifically, hydraulic conductivity after breakthrough events (Figure 2-6) and swelling pressure (Figure 2-7) after fast gas breakthrough tests were observed.

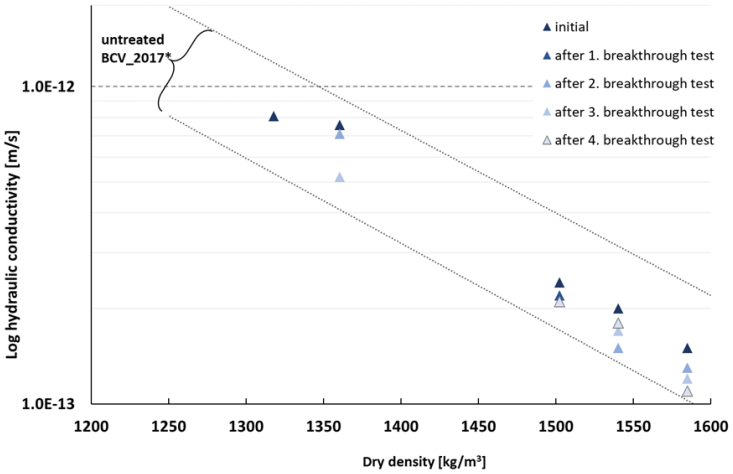

*Figure 2-6 – Hydraulic conductivity (at 10°C) after the fast gas breakthrough tests and resaturation phase for samples of BCV bentonite with the artificial joint in comparison with an initial values (*data from Šachlová, 2022).*

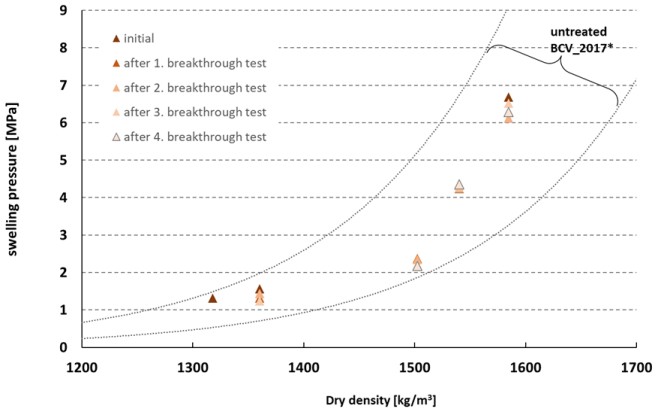

*Figure 2-7 – Swelling pressure after fast gas breakthrough tests and resaturation phase for the samples of BCV bentonite with the artificial joint (*data from Šachlová, 2022).*

When comparing results obtained with an artificial joint (Figure 2-6 and Figure 2-7) and without joint (Figure 2-4 and Figure 2-5), one sees that the presence of the joint has a very limited to no effect on both the swelling pressure and water permeability.

Even after several gas breakthrough and the creation of dilatant pathways, self-sealing occurs. It can be observed a reduced impact of gas events on water permeability and even a low diminution of it that could be representative of a compaction of the material due to high gas pressure.

2.2.3 Conclusion

Constant volume cells were used to conduct the experimental program, allowing fully saturation of the sample and measurement of swelling pressure and hydraulic conductivity. The experiments used powdered Czech Ca-Mg bentonite compacted to different dry densities.

The experimental process included multiple cycles of sample (re)saturation, hydraulic conductivity measurement, and gas breakthrough testing. After the testing was completed, the cells were dismantled and various sample characteristics, such as water content, density, and dry density, were determined. The experimental tests were performed on two sets of specimens: homogeneous samples and samples with artificial joints. Batches of samples with varying dry densities were tested for each set.

The first set of tests were conducted on homogeneous BCV bentonite samples with varying dry densities, ranging from 1290 to 1510 kg/m³. The primary focus was on the evaluation of the hydraulic conductivity, swelling pressure, of the samples during and after the fast gas breakthrough tests and endurance (time required to obtain the breakthrough event). The experiments lasted over a year for each sample, with five fast gas breakthrough tests, and resaturation phases lasting three or six months.

All the tests displayed minimal changes in both hydraulic conductivity and total stress after fast gas tests. Slight variations are observed depending on initial dry density. A minor and moderate long-term decrease in hydraulic conductivity occurred during the testing period. Time required to gas breakthrough increased with the higher dry density, indicating greater resistance and evolved with time without clear time dependence law. These slight evolutions of permeability, total stress and time to reach gas breakthrough suggest possible evolution of the material. In any case, gas injection/breakthrough to not alter the basic HM properties of the bentonite samples.

The second set of experiments involved five samples with an artificial longitudinal joint made of BCV bentonite, with dry densities ranging from 1318 to 1585 kg/m³. These samples were subjected to a series

of tests to assess hydraulic conductivity, swelling pressure, and endurance during and after fast gas breakthrough tests. After an initial saturation phase lasting about 6 months for each sample, cyclic loading was initiated, and a fast gas breakthrough test was performed.

Samples were tested for several months, involving four/five loading cycles. As observed on the homogeneous samples, hydraulic conductivity decreased with an amplitude depending on the dry density (Figure 2-6). Total stress was not significantly affected by cyclic loading.. A change in endurance was observed in each test but as in the case of homogeneous samples, due to a behaviour not systematic, it is difficult to conclude on the reason of these differences in gas breakthrough time.

The results of these experiments provide valuable insights into the behaviour of BCV bentonite samples (in homogeneous condition and with artificial joint) under the fast gas breakthrough conditions, emphasising hydraulic conductivity, swelling pressure, endurance, and episode as key parameters. Joint in bentonite block do not alter the performances of the material expected for EBS and the properties are similar to the one obtained on homogeneous samples. Multiple gas breakthrough events in both materials (with joint or homogeneous) do not affect the HM characteristics suggesting an efficiency of self-sealing even after creating dilatant pathways.

2.3 Laboratory tests on clay host rocks

Three clay formations considered as suitable host rocks for the deep geological disposal of radioactive waste have been studied in the GAS and HITEC work packages: the Boom Clay in Belgium, the Callovo-Oxfordian (Cox) in France and the Opalinus Clay in Switzerland. A short comparison of the mineralogical composition of these rocks is shown in Table 2-2, reference is made to the SotAs (Levasseur et al, 2021 and Villar et al., 2023) for more detailed information.

Table 2-2 – Mineralogical composition of the clay host rocks (Villar et al., 2023)

Mineral (%)	Boom Clay	Cox (UA2)	Opalinus
Clay minerals		24 – 52 (52)	>40
Illite	5 – 11	8 – 20 (17)	23
Smectite + Interstratified illite/smectite	7+7 – 17+25	15 – 30 (28)	12
Kaolinite	1 – 6	0 – 4 (4)	18
Chlorite	1 – 3	1 – 3 (3)	8
Interstratified chlorite/smectite	0 – 5		0
Interstratified kaolinite/smectite	1 -- 6		
Quartz	20 – 52	15 – 26 (17)	20
K-Feldspars	3 – 9	1 (1)	2
Plagioclase	1 – 5	1 (1)	1
Carbonates		24 – 46 (26)	
Calcite	0 – 6	20 – 40 (22)	14
Siderite	0 -- 4	Present	3
Dolomite	0 -- 1	3 – 8 (4)	<1
Ankerite			
Muscovite	5 -- 9		
Pyrite	0 -- 4	1 – 3 (1)	<1
Organic Carbon	0 – 5	0.5 – 1	1
Others			
Gypsum	0 -- 1	Present	
Glauconite, apatite, rutile, anatase, ilmenite	Present	Present	
Zircon, monazite, xenotime			

Table 2-3 shows which clay rocks were studied by the different laboratories in the GAS and HITEC work packages.

Table 2-3 – Self-sealing tests on clay rocks performed in the GAS (G) and HITEC (H) work packages

	BGS	CIMNE/UPC	EPFL	GRS	UGrenoble	ULorraine
Boom Clay	G	G				
Callovo-Oxfordian	G H			G	H	G H
Opalinus Clay	G H		G	G		

2.3.1 ULorraine (CNRS) - Self-sealing tests in triaxial cell

ULorraine developed an experimental device (X-rays transparent triaxial compression cells) procedure in complementarity of WP7-HITEC (Sub-task 2.1) and WP6-GAS (Sub-task 3.2). In WP7, the impact of temperature on self-sealing process and water permeability of macroscopic (artificial) fracture is studied. In WP6, the impact of self-sealing and temperature on water/gas permeability of macroscopic (artificial) fracture is studied.

2.3.1.1 Description of the tests and experimental set up

The thermo-hydro-mechanical self-sealing experiments were performed on cylindrical samples in newly developed (for the EURAD project) triaxial compression cells with heating system and a new deformations monitoring system (fiber optics). The cells body is made of PEEK, an X-ray transparent polycarbonate, thus allowing X-rays 3D scans during hydromechanical tests. It allows applying high isotropic and deviatoric stresses on cylindrical samples.

The cell is put in an X-ray tomograph, as illustrated in Figure 2-8. The voxel resolution is about 20-30 µm, depending on size of triaxial cell and sample. Visualization and analysis of CT voxel data will be performed using VGStudio MAX software (Volume Graphics GmbH), allowing precise analysis of voxel data. Hence, the volume of damage-induced cracks can be determined by image analysis.

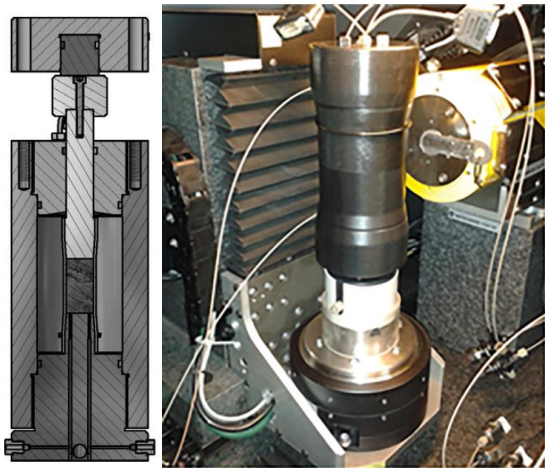

Figure 2-8 – Left: schematic representation of a triaxial compression cell made of PEEK with a cylindrical sample of 20 mm diameter for self-sealing and fracturing tests. Right: the triaxial compression cell in a X-ray nano-tomograph.

Experimental procedure

Cylindrical samples were cut along two orientations, parallel and perpendicular to the bedding plane. For these self-sealing tests, samples of 20 mm diameter and 40 mm height were used in the first PEEK triaxial cell and deformations were measured. Cracks (opening = 0.4 mm) were generated artificially by sawing and milling (*Figure 2-9*).

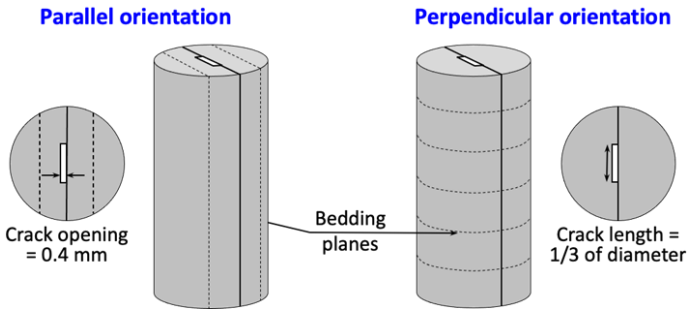

Figure 2-9 – Geometry of the artificially cracked cylindrical samples (diameter 20 mm, height 40 mm)

The low confining pressure (4 MPa) considered for these tests mimics the pressure applied on the galleries wall by swelling clays (bentonite) of the plug.

Main test sequences for self-sealing tests

The self-sealing tests were performed on fractured cylindrical samples (macroscopic and localized fracture). During the self-sealing tests in the GAS WP experiments, water and gas will be injected in the fractured samples and permeability will be measured continuously.

Table 2-4 – Comparison of the main test sequences for the HITEC and GAS self-sealing experiments

HITEC (2.1) self-sealing	GAS (3.2) self-sealing
• A naturally saturated sample is artificially fractured (crack opening = 0.4 mm) and then put in the triaxial cell and isotropic stresses (4 MPa) are applied to the samples. • The temperature is increased until the selected value (40 °C, 60°C, 80 °C, 100 °C). • The triaxial cell is installed in the X-ray tomograph and the initial 3D scan is performed. • Saturation of the fracture with the synthetic water of Andra at a flow rate of 0.05 ml/min. • Water percolation under pressure (Pin = 1 MPa, Pout = 0.8 MPa) in the fracture at a flow rate of 0.02 ml/min during 2 months. Water permeability of the fracture is measured continuously. • 3D scans are performed at t = 1, 2, 3, 4, 5, 10, 15, 20, 30, 60 days.	• A naturally saturated sample is artificially fractured (crack opening = 0.4 mm) and then put in the triaxial cell and isotropic stresses (4 MPa) are applied to the samples. • The triaxial cell is installed in the X-ray tomograph and the initial 3D scan is performed. • Saturation of the cracks with the synthetic water of Andra at a flow rate of 0.05 ml/min. • Water percolation under pressure (Pin = 1 MPa, Pout = 0.8 MPa) in the fracture at a flow rate of 0.02 ml/min during 2 months. Water permeability of the fracture is measured continuously, while gas permeability is measured punctually. • 3D scans are performed each day during the first 5 days, and then each five days.

2.3.1.2 Results and discussion

A total of 12 samples were tested in the GAS and HITEC work packages and in a previous project for Andra. These cores come from the Clay Unit (UA) that will host the repository and from the more carbonate-rich Silty-Carbonate Unit (USC) in the upper part of the Cox formation. The references of the different samples with corresponding characteristics and experimental conditions are given in Table 2-5. Each self-sealing test lasted at least one month.

Table 2-5 – References of the different samples with corresponding characteristics and experimental conditions

Samples	Unité	%$CaCO_3$	Solid grain density (g/cm^3)	Fracture opening (µm)	Orientation	Temperature (°C)
EST60018-71	UA	5	2.61	400	⊥	20
EST60766-3	UA	21	2.67	400	//	20
EST62690-2	UA	21	2.67	800	//	20
EST66723-11	UA	21	2.66	400	⊥	20 / GI
EST66723-12	UA	21	2.66	400	⊥	80
EST66727-05	UA	21	2.68	400	//	40
EST66418-5	UA	25	2.69	400	//	20 / GI
EST66418-10	UA	25	2.69	400	//	80
EST63744-7	UA	32	2.69	400	//	20
EST63744-11	UA	32	2.69	400	⊥	20
EST60007-71	USC	53	2.71	400	⊥	20
EST59996-71	USC	68	2.71	400	⊥	20

The impact of the following parameters on the self-sealing potential of the Cox claystone were studied:

- Sample orientation
- Calcite content
- Crack aperture
- Temperature
- Gas injection

The self-sealing process is evaluated by permeability measurements (*Figure 2-10*) and with the evolution of the crack volume from the X-ray tomography 3D images (*Figure 2-11Figure 2-10*). For samples with very low and high calcite content, no permeability measurements could be performed as the fracture respectively closed very fast or did not close at all, and only the crack volume could be used.

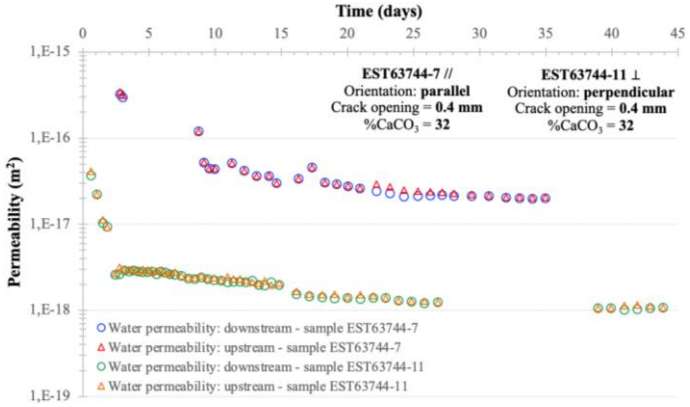

Figure 2-10 – Evolution of water permeability of parallel sample EST63744-7 and perpendicular sample EST63744-11 during self-sealing test at 20°C

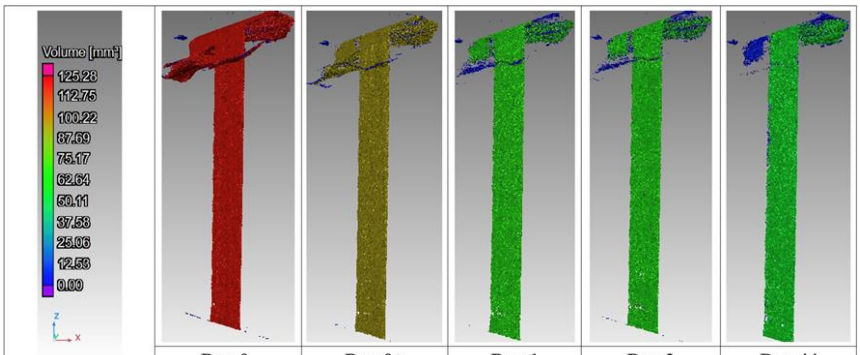

	Day 0-	Day 0+	Day 1	Day 2	Day 44
Volume (mm³)	126.2	96.0	70.7	69.4	60.8
%CaCO₃	32				

Figure 2-11 – X-ray 3D tomography images of perpendicular sample EST63744-11 showing the evolution of the crack volume with time (initial crack opening = 0.4 mm) during self-sealing test at 20°C (Day 0-: after hydrostatic loading; Day 0+: after crack saturation)

Figure 2-12 represents the volume variation of the crack (normalized by the initial crack volume after hydrostatic loading) obtained from X-ray tomography 3D images during all self-sealing tests with water, for parallel (left plot) and perpendicular orientations (right plot). Whatever the sample orientation (parallel or perpendicular), the initial crack opening and the test temperature, a similar trend is observed and the calcite content appears to have the highest impact on the self-sealing efficiency.

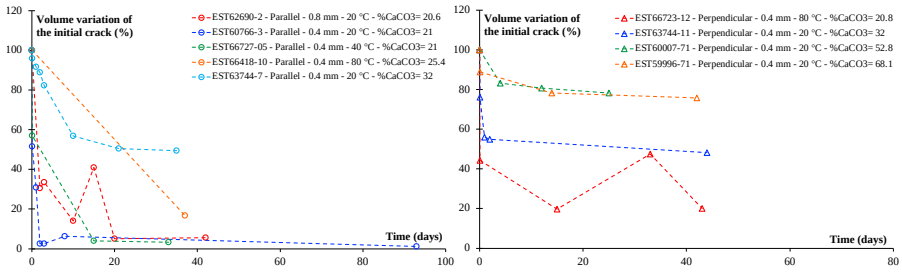

Figure 2-12 –volume variation percentage of the initial crack (normalized with the volume after hydrostatic loading) obtained from X-ray tomography 3D images during all self-sealing tests with water, for parallel (left) and perpendicular (right) orientations.

Figure 2-14 represents the volume variation of the initial crack at the end of the test as a function of the calcite content for both orientations. It shows that the self-sealing capacity is strongly correlated to the calcite content. This result highlights the importance of the mineralogy (i.e., clay and carbonate content) of the clay host rock to allow a good sealing of fractures in the EDZ during the resaturation of the underground structures for radioactive waste storage in clayey rocks, which will guarantee the safety of the site.

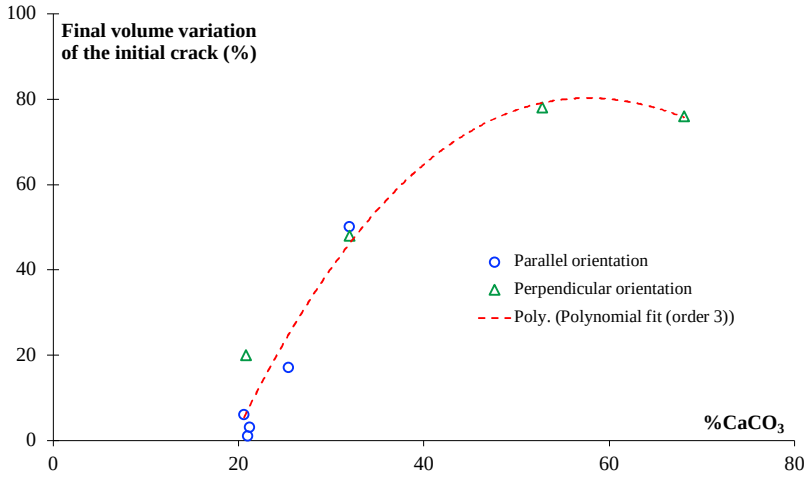

Figure 2-13 – Volume variation percentage of the initial crack at the end of the test as a function of the calcite content for both orientations.

2.3.1.2.1 Influence of temperature on the self-sealing process

The influence of temperature on the self-sealing process has been studied by performing self-sealing tests at temperatures up to 80 °C following the protocol described previously. The following samples have been tested:

- Parallel sample EST66418-10 with an artificial fracture of 0.4 mm and a carbonate content of 25.4%, at T = 80 °C
- Parallel sample EST66727-05 with an artificial fracture of 0.4 mm and a carbonate content of 21%, at T = 40 °C

- Perpendicular sample EST66723-12 with an artificial fracture of 400 µm and a carbonate content of 20.8%, at T = 80 °C

The evolution of the water permeability during the self-sealing tests performed on parallel samples EST66418-10 (25% calcite) tested at 80°C and EST66727-5 (21% calcite) at 40°C is presented in *Figure 2-14* (left) and compared with the curves of the sample EST60766-3 and EST63744-7 that are similar (with respectively 21% and 32% calcite) but performed at ambient temperature (20°C). An increase of the water permeability just after the heating at 80 °C is observed for sample EST66418-10, followed by a fast and then moderate decrease of the water permeability. Just after this rapid decrease, the water permeability drop follows then the water permeability drop pattern observed in the other tests at room temperature. In sample EST66727-05 tested at 40°C, the water permeability evolves almost in the same way as for the sample EST60766-3 performed at 20°C.

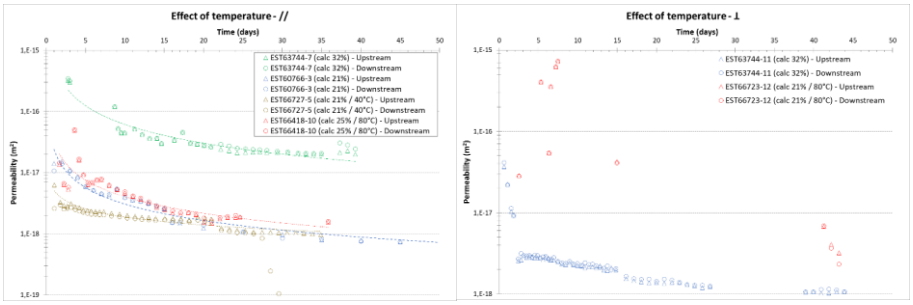

Figure 2-14 – Evolution of water permeability during self-sealing tests at different temperatures on parallel samples (left) and perpendicular samples (right)

Concerning the perpendicular orientation, no good water permeability measurements of the fracture could be performed in sample EST66723-12 that was tested at 80°C, because of plugged capillary issues. However, self-sealing process was efficient, as illustrated in *Figure 2-15* which shows the evolution of the fracture geometry obtained from the 3D X-ray tomography data. Before water saturation (just after hydrostatic loading), the fracture volume was equal to 44 mm³. Just after crack saturation, it decreased to about 19 mm³. After 43 days of self-sealing experiment, the volume decreased down to 9 mm³.

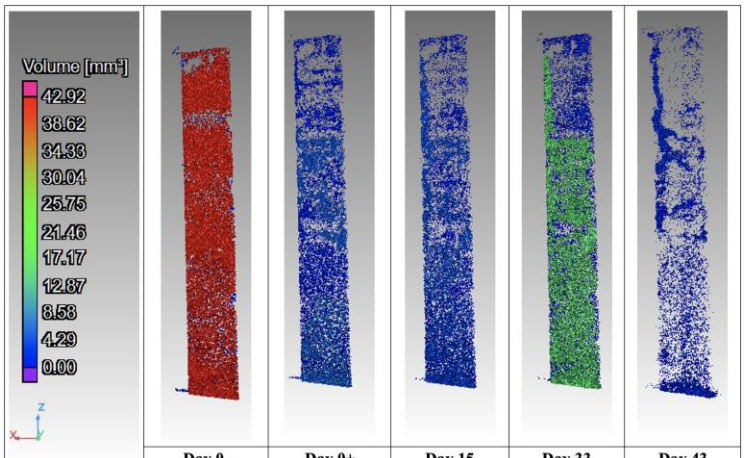

	Day 0-	Day 0+	Day 15	Day 33	Day 43
Volume (mm³)	43.9	19.4	8.7	20.9	8.8
%$CaCO_3$	20.8				

Figure 2-15 – 3D X-ray tomography images of perpendicular sample EST66723-12 showing the evolution of the crack volume with time (initial crack opening = 0.4 mm) during the self-sealing test at 80 °C (Day 0-: after hydrostatic loading; Day 0+: after crack saturation)

The rapid permeability increase observed after heating in parallel sample EST66418-10 may be explained by the water overpressure inside the fracture, which spreads the fracture lips and thus increases the water permeability of the fracture. The coefficient of thermal expansion of water (2.6×10^{-4} $(°C)^{-1}$ at 25 °C and 5.8×10^{-4} $(°C)^{-1}$ at 80 °C) is actually an order of magnitude greater than that of solid grains in the Cox claystone (2.6×10^{-5} $(°C)^{-1}$ at 25 °C and 11×10^{-5} $(°C)^{-1}$ at 80 °C) (Mohajerani, 2011). The pore water overpressure induced by heating inside the fracture dissipates quickly afterwards, as soon as drained conditions are restored. Thereafter, the permeability evolution behaves like for the other tests, i.e., decreases first rapidly, then slowly (*Figure 2-14*). It is worth emphasizing that the variation of water viscosity with temperature was taken into account in the permeability calculations.

No such permeability increase was observed on sample EST66727-05 heated to 40°C; this temperature rise was probably not sufficient to expand the crack and affect its permeability.

2.3.1.2.2 Influence of gas injection on the self-sealing process

We compare here the results obtained from two self-sealing tests (a parallel sample EST66418-5 with 25.4% $CaCO_3$ and a perpendicular sample EST66723-11 with 20.8% $CaCO_3$) with water and gas injection with the results of 3 self-sealing tests performed within the Task 2 of HITEC WP with only water injection: EST60766-3 (parallel, 21% $CaCO_3$), EST63744-7 (parallel, 32% CaCO3), EST63744-11 (perpendicular, 32% $CaCO_3$). The initial crack opening is the same for all these samples (0.4 mm). The evolution of the water permeability is presented in *Figure 2-16*.

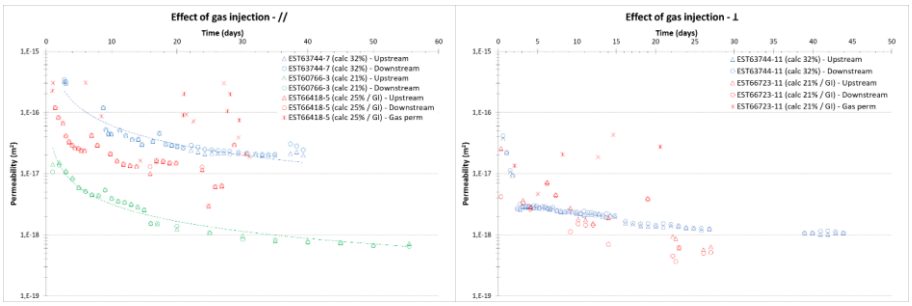

Figure 2-16 – Evolution of water permeability during self-sealing tests with only water and with both water and gas injection on parallel samples (left) and perpendicular samples (right)

The scattering of gas permeability measurements may be explained by: (i) the difficulty to obtain a measurable steady state gas flow (the time interval is not the same for all gas permeability measurements), (ii) the difficulty to apply and measure precisely low gas pressures at the bottom/upstream of the triaxial cell, (iii) the residual water inside the crack that can disturb the gas flow.

At the end of the self-sealing test on the parallel sample EST66418-5, the water permeability is equal to $6x10^{-18}$ m^2, whereas the gas permeability is about 10^{-16} m^2. At the end of the self-sealing test on the perpendicular sample EST66723-11, the water permeability is equal to $6x10^{-19}$ m^2, whereas the gas permeability is about 10^{-17} m^2. In both cases, the water permeability decreases quite rapidly at the beginning like for the other tests but the decrease is slower thereafter. In addition, for both orientation, there is a very significant closure of the crack. Gas injections induce each time some desaturation of the crack but there is no evidence for a significant slow-down of the decrease in the water permeability and a significant reduction of the self-sealing process. This result has to be confirmed by additional similar experiments and, more important, with longer experimental run times and longer gas injection durations.

Indeed, in that case, the long-term injection of an inert gas may have a retarding effect on the self-sealing process.

The GAS and HITEC tests at 80°C were performed on samples cut from the same cores and give an opportunity to compare the relative impact of temperature and gas injection on the self-sealing ability. For samples cut parallel to bedding (*Figure 2-17*, left), the gas injection seems to have a detrimental or delay effect compared to heating. However, most of the difference appears at the initial loading and saturation steps, the trends are afterwards similar. For the perpendicular orientation (*Figure 2-17*, right), the quality of the permeability measurements in the HITEC tests is not good enough to make a comparison.

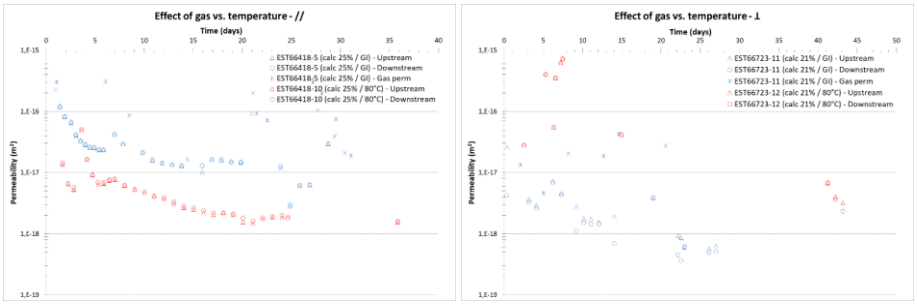

Figure 2-17 – Evolution of water permeability during self-sealing tests with only water on heated samples and with both water and gas injection on parallel samples (left) and perpendicular samples (right)

2.3.1.3 Conclusion

Self-sealing experiments have been performed in triaxial compression cells under X-ray tomography on artificially fractured (with parallel and perpendicular orientations) samples of the Cox claystone. 3D X-ray scans have been performed on all tested samples before, during and after the experiments. The voxel data have been analyzed with a specific software for the visualization and analysis of computed tomography (CT) data in order to assess the evolution of the crack volume. Fracture permeability (to water and gas) was measured continuously during all tests.

The focus was to study the impact of gas injections on the self-sealing process. We compared the results from these two self-sealing tests with water and gas injection with those obtained from five self-sealing tests (with both orientations and different calcite contents) performed within the Task 2 of HITEC WP with only water injection. Self-sealing tests were carried out at room temperature (20°C) and lasted at least one month. Generally speaking, the higher the calcite content, the less effective the self-sealing process, whatever the sample orientation (parallel or perpendicular). An effective sealing requires a carbonate content lower than 40%. Moreover, it seems that the self-sealing process is equally efficient for both parallel and perpendicular orientations. Generally, the self-sealing process is fast at the beginning of the test and then stabilizes after one month. The permeability of the Cox claystone samples is partially restored compared to the initial permeability of the healthy claystone and the initial crack is very significantly closed at the end of the self-sealing experiment. These first results are very promising and give confidence to the positive impact of the self-sealing process on the restoration of the initial hydraulic (i.e., sealing) properties of the Cox claystone. It is all the more promising that the duration of our experiments is much shorter than the in-situ time scale. This physico-chemical mechanism will allow a good sealing of fractures in the EDZ during the resaturation of the underground structures for radioactive waste storage, which will guarantee the safety of the site. Gas injections induce each time the desaturation of the crack but there is no evidence for a significant slow-down of the decrease in the water permeability and a significant reduction of the self-sealing process. These first results are also very promising and give confidence to the positive impact of the self-sealing process even if there is a gas flow. However, they have obviously to be confirmed by additional similar experiments and, more

important, with longer experimental run times and longer gas injection durations. Indeed, in the latter case, the long-term injection of an inert gas could have a retarding effect on the self-sealing process.

For Auvray et al. (2015) and Giot et al. (2019), three main processes are involved in self-sealing. The first is swelling between smectite sheets (intra-particle or crystalline swelling) due to adsorption of water since the samples are a little desaturated initially. The second is inter-particle swelling due to osmotic effects by absorption of water between clay particles at higher water saturation (i.e., during self-sealing experiment). The last is plugging of the fractures by particle aggregation. Water penetrates more easily between the clay sheets in samples oriented parallel to the bedding plane, thus initiating the self-sealing process more quickly. During these quick phases, there is a rapid decrease of the water permeability and the crack volume (*Figure 2-16*). Then, there is a moderate and progressive decrease in water permeability and crack volume (*Figure 2-12*) due to the progressive swelling of smectite clay minerals in the whole sample and the expansion and densification of clay plugs in the central crack. For parallel samples, clay minerals can swell freely laterally towards the inside of the fracture without any constraint whereas for perpendicular samples, the axial contraction (due to the 4MPa confining pressure) prevents probably a free swelling of the clay minerals surfaces in the axial direction. From these first results, it seems surprising that the self-sealing process is not more efficient for the parallel sample (i.e., when the bedding plane is parallel to the fracture surface). The (crystalline and osmotic) swelling mechanisms are certainly more efficient for the parallel samples, but the final phases of plugs formation, expansion and densification, which are maybe less dependent on the sample orientation, are possibly much more efficient to seal cracks.

The water permeability of clayey facies samples decreased significantly during self-sealing tests: from 10^{-17} to 7.10^{-19} m^2 in 55 days for sample EST60766-3, from 3.10^{-16} to 2.10^{-17} m^2 in 35 days for sample EST63744-7, from 4.10^{-17} to 1.10^{-18} m^2 in 44 days for sample EST63744-11. However, the initial permeability of the healthy (i.e., initial) claystone, which is almost two orders of magnitude lower (10^{-20} m^2 to 10^{-21} m^2) according to previous works (Escoffier 2002, Homand et al. 2004, Grgic et al., 2023), is not recovered on the time scale of the experiment (below two months). Moreover, the self-sealing process induces a significant reduction of the crack volume (*Figure 2-16*). Concerning the samples with high calcium carbonate content (EST60007-71 and EST59996-71), self-sealing was very moderate and the fracture remained globally open (*Figure 2-13*). The calcite content, which is roughly anti-correlated with the clay content, has therefore a strong impact on the physico-chemical sealing process in claystone. The higher the carbonate content, the slower the self-sealing process, whatever the sample orientation. These results support the work of Giot et al. (2019) where it is indicated that the threshold regarding the carbonate content to observe an effective self-sealing would be around 40%, results obtained on small samples. This result highlights the importance of the mineralogy of the clay host rock to allow a good sealing of fractures in the EDZ during the resaturation of the underground structures for radioactive waste storage in clayey rocks.

2.3.2 UKRI- BGS - Self-sealing tests in shear ring

Direct shear box testing forms part of the test programme over both WP HITEC and WP GAS. Despite these test programmes being significantly different there are still cross overs which can be seen between the two test programmes. The shear tests as part of HITEC investigated the effect of temperature on fracture mechanics and self-sealing. It has been proposed between Andra and BGS that during testing on the Callovo-Oxfordian claystone a small phase of gas injection would be carried out towards the end of the elevated temperature shear test. This would have provided a database of gas transmissivity to be compared against the data gathered during the WP GAS project. These tests could unfortunately not be performed due to Covid and time constraints.

2.3.2.1 Description of the tests and experimental setup

A series of direct shear experiments were performed. Figure 2-18 shows a schematic of the test layout of the Direct Shear Rig (DSR). Cylindrical samples of 60 ± 0.1 mm diameter and 53 ± 1 mm height are rigidly housed within two steel collars. The sample can be loaded vertically up to 34.7 MPa by means of

a hydraulic ram, which is actuated using an ISCO/Teledyne 260D syringe pump. Load is measured by two Applied Measurements Limited load cells (DBBW-5T) with an accuracy of ± 0.01 MPa and vertical displacement by a MicroSense 4810/2810 induction sensor with a full range of ±0.5 mm and an accuracy of ±0.06 µm. Horizontal stress is created by the Poisson's effect in response to vertical loading in a K0 geometry. The sample is sheared by means of a second (500D) syringe pump, which has been modified to directly shear the sample along a low-friction track. Shear stress transmitted through the sample/fracture is measured by a 50 kN rated load cell (17.6 MPa) with an accuracy of 0.01 MPa. Horizontal movement of the shear water bath is measured by a linear variable differential transformer (LVDT), which has a full range of ±25 mm and an accuracy of 0.5 µm. Constant displacement shear can occur at rates as slow as 14 microns a day (equivalent to 1 mm in 69 days) or as fast as 0.5 mm per second. Fluid is injected directly to the fracture through a 4 mm bore drilled to the fracture plane, which has a porous plastic filter at the end. Pore pressure is controlled by a third (500D) syringe pump.

For the injection of gas, a 1,000 ml water/gas interface vessel is used. Injection pressure is kept constant measured using a Gems 3100 series pressure transducer with a maximum range of 10 MPa and an accuracy of ±0.025 MPa. All three syringe pumps recorded pressure (±0.003 MPa), flow rate (±0.25 µl/h), and volume (±1 µl).

Temperature is created by four RSPro cartridge heaters that are to be placed into the rig, these will be controlled by a close control system to provide a constant heat to the sample.

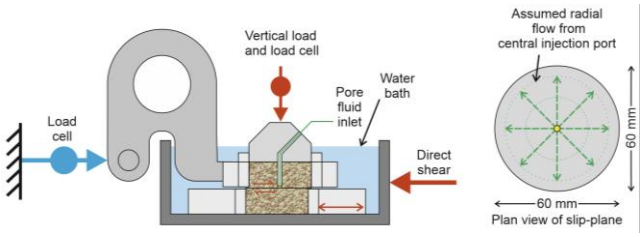

Figure 2-18 – Experimental set-up for water/gas testing with radial constraint and axial strain measurements

The test protocols are described in detail in GAS deliverable 6.8 and in HITEC deliverable 7.3.

2.3.2.2 Results and discussion

At the time of reporting, a total of 13 shear experiments have been completed in the HITEC test programme. This included all the experiments planned in Opalinus Clay and enough experiments in Callovo-Oxfordian claystone to make statements about the influence of temperature on shear properties and flow. None of the experiments using Boom Clay had been conducted.

Table 2-6 – Summary of experiments completed in the HITEC WP. Note: tests in red have yet to be conducted and will be complete by the end of the project.

Rock type	Normal load (MPa)	Pore pressure (MPa)	Temperature of initial shear	Status
Opalinus Clay	3.6	1	Ambient	1 2 3 4 5
	3.6	1	Raised	45 67 90
Callovo-Oxfordian	3.6	1	Ambient	1 2 3 4 5
	3.6	1	Raised	45 67 90

Boom Clay	3	1	Ambient	1 2
	3	1	Raised	45 67 90

The experimental programme was late to start because of the Covid-19 pandemic and delays to the modification of the apparatus. None of the experiments using Boom Clay had been conducted. Each experiment took around two weeks to complete. The initial shearing of intact samples took around 1 day, followed by one week of hydraulic flow into the fracture, and a further week with continued hydraulic flow while the sample was actively sheared.

On the other hand, most tests planned on the host rocks in the GAS WP were completed (Table 2-7).

Table 2-7 – Experimental programme. Note: tests in red are not conducted in time for reporting but will be complete by the end of the EURAD-GAS project

Rock	Normal load (MPa)	Pore pressure (MPa)	Shear orientation	Number of tests
Boom Clay	5.1	1	Parallel	1 2 3
	3	1	Parallel	1 2 3
Callovo-Oxfordian claystone	7.1	1	Parallel	1 2 3
	7.1	1	Perpendicular	1 2 3
Opalinus Clay	4	1	Parallel	1 2 3
	4	1	Perpendicular	1 2 3
Synthetics[#]	4	1	Parallel	1 2 3 4 5 6

A similar testing protocol was applied in the GAS and HITEC work packages (Table 2-8).

Table 2-8 – Description of test stages for the GAS and HITEC experiments

GAS		HITEC	
Stage	**Detail**	**Stage**	**Detail**
Sample loading	Sample weighed and measured, wrapped in cling film, and loaded into two steel rings. Sample loaded into the DSR, and normal load increased in a series of steps to target stress.	**Sample loading**	Sample weighed and measured, wrapped in cling film, and loaded into two steel rings. Sample loaded into the HSR and normal load increased in a series of steps to target stress. Temperature established and equilibrated.
Intact shear	Intact sample sheared at constant rate to create a realistic fracture.	**Intact shear**	Intact sample sheared at constant rate to create a realistic fracture.
Fracture scanning	Both fracture surfaces were laser scanned to determine fracture topology. Top fracture had a 4mm hole drilled to allow the addition of	**Fracture scanning**	Both fracture surfaces were laser scanned to determine fracture topology. Top fracture had a 4mm hole drilled to allow the addition of an

	an injection bore directly to the fracture plane.		injection bore directly to the fracture plane.
Initial gas flow	Constant gas pressure of 1 MPa created, and flow monitored	**Sample reloading**	Sample re-loaded into the apparatus. Normal load and temperature established.
Hydraulic flow	Injection of synthetic pore water (Levasseur et al, 2021) at a constant pressure of 1 MPa	**Hydraulic flow**	Injection of synthetic pore water at a constant pressure of 1 MPa
Repeat gas flow	Constant gas pressure of 1 MPa created, and flow monitored	**Repeat shear**	Sample re-sheared at a constant rate and water flow monitored. Comparing the water flow rate of Stage 5 with Stage 6 determined the self-sealing capacity of the fracture to shear displacement
Repeat shear	Sample re-sheared at a constant rate and gas flow monitored		
Repeat fracture scanning	Both fracture surfaces were laser scanned to determine fracture topology.	**Repeat fracture scanning**	Both fracture surfaces were laser scanned to determine fracture topology.

2.3.2.2.1 Calculation of self-sealing potential (SSP)

Experience has shown that there is considerable variation in flow in repeat experiments, up to three orders of magnitude. The fracture topology is measured to ascertain whether variation in flow is related to the surface characteristics of the fracture. However, flow is likely to be associated with asperities and fracture roughness is not a measure of mismatch between the top and bottom fracture surface and therefore an estimate of the properties of asperities.

The GAS experiment was designed to determine four different flow magnitudes; initial gas flow, hydraulic flow, repeat gas flow, and gas flow during shearing. From these four parameters it was aimed to determine the change in flow as a result of (1) hydration of the fracture and (2) shear along the fracture. The change in flow determines the self-sealing potential of the rock. Therefore, self-sealing potential is defined as:

$$SSP_{H2O} = \frac{Flow\ of\ gas_{initial}}{Flow\ of\ gas_{repeat}} \quad \text{and} \quad SSP_t = \frac{Flow\ of\ gas_{repeat}}{Flow\ of\ gas_{shear}}$$

The HITEC experiment was designed to determine three different flow magnitudes: initial water flow, steady water flow, and water flow during shearing. The self-sealing potential is then defined as:

$$SSP_{H2O} = \frac{Flow\ of\ water_{initial}}{Flow\ of\ water_{steady}} \quad \text{and} \quad SSP_t = \frac{Flow\ of\ water_{steady}}{Flow\ of\ water_{shear}}$$

These measures of self-sealing potential remove the variation in flow and define a proportional variation. It is still expected that variation will exist but that this approach removes a large part of the variation. It should be noted that SSP > 1 means that gas flow is reduced. Therefore, a SSP_{H2O} of 2 means that hydration of the fracture has resulted in a halving of the gas flow. Conversely, SSP < 1 means that flow has increased. Therefore, an SSP_t of 0.5 means that flow has doubled because of shearing.

2.3.2.2.2 Main results

Figure 2-19 compares the GAS results for all three rock-types, showing Self-Sealing Potential (SSP) on the same y-axis scale. All tested conditions showed either a reduction or no change in gas flow because of hydration of the fracture. The influence of water on gas flow was greatest for Opalinus Clay, with over one order of magnitude greater SSP than Callovo-Oxfordian claystone, the latter only having a moderate decrease in flow as a result of hydration. Opalinus Clay had nearly two-orders of magnitude reduction in flow as a result of injection of water on the fracture. In Boom Clay, the full story is more complex.

Discounting the one test that showed considerable SSPH20 after the fracture would initially not hold gas pressure, the two other tests at the Belgian depth range showed a modest increase in gas flow. Therefore, small volumes of excess water on the fracture plane enhances gas flow. Figure 2-19 shows that there is considerable difference in SSP_{H20} between rock types, but there is limited variation within the rock types that were sheared at different directions. Shearing showed either no change, or an increase in flow.

The Callovo-Oxfordian claystone and the Opalinus Clay were tested with two different orientations, with bedding either parallel or perpendicular to the shear direction. The Boom Clay on the other hand was tested at a stress representative of the Belgian disposal concept (220m depth) and of the Netherlands disposal concept (500m).

In Opalinus Clay no change in flow was seen for shearing parallel with bedding, with a modest increase for samples oriented perpendicular to bedding. In Boom Clay, only a modest increase was seen, with little variation based on the depth of study. Almost all the five tests conducted in Callovo-Oxfordian claystone showed an increase in flow of around one order of magnitude. Table 2-9 summarises the conclusions of the flow results, with entries shown in red indicating an increase in flow (SSP < 1) and entries in green showing a decrease in flow (SSP > 1). If sealing is desired, SSP > 1 is preferable.

Table 2-9 – GAS Self-Sealing Potential (SSP) conclusion. Note # - increase seen when one test with high degree of sealing is discounted.

Rock Type	Condition	Hydration		Shear	
Boom Clay	220m	Increase[#]	0.6	Increase	0.4
	500m	No change	1.5	Increase	0.4
Callovo-Oxfordian claystone	Parallel	Decrease	3.8	Increase	0.06
	Perpendicular	Decrease	4.3	Increase	0.04
Opalinus Clay	Parallel	Decrease	38	No Change	0.8
	Perpendicular	Decrease	133	Increase	0.3

a mis en forme le tableau

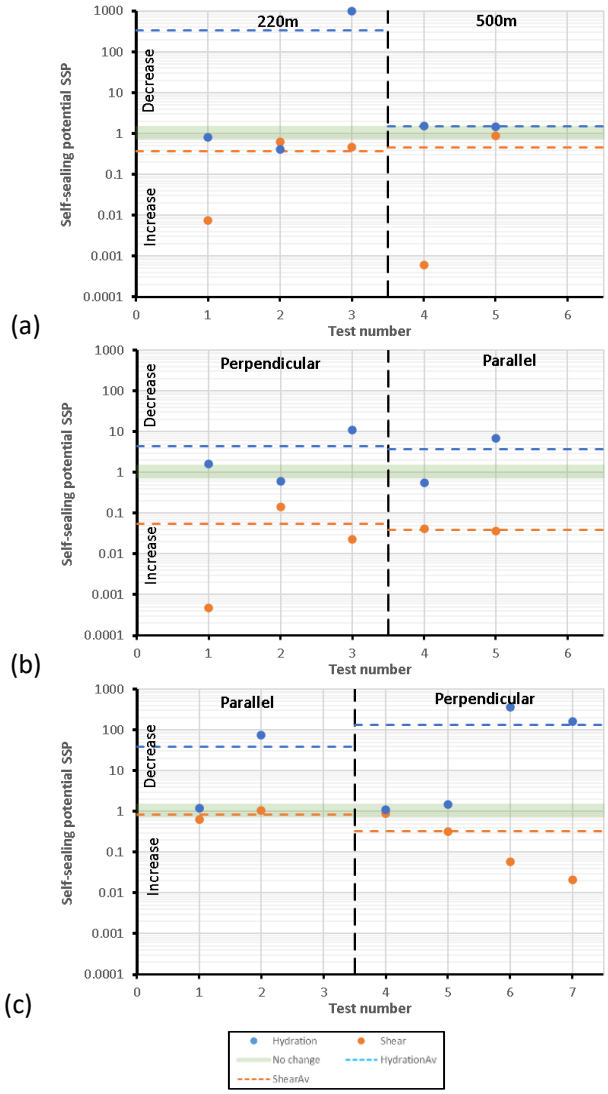

Figure 2-19 – Self-Sealing Potential (SSP). a) Boom Clay; b) Callovo-Oxfordian claystone; c) Opalinus Clay.

2.3.2.2.3 Effect of temperature on the self-sealing potential

Figure 2-20 shows the results of self-sealing potential in Opalinus Clay. Figure 2-20a shows the results of self-sealing potential as a result of hydration (SSP_{H2O}). All tests showed a reduction in flow, therefore all results have a magnitude greater than 1. Two sets of data are displayed. The blue circles show the data for fractures that were initially fractured at ambient temperature, while the red circles show the data that were initially sheared, and subsequently re-sheared, at elevated temperature. Both show a similar relationship, with self-sealing potential reducing with temperature. However, samples that are fractured at temperature have a greater self-sealing potential than those sheared at ambient temperature. Figure

2-20b also shows a reduction in self-sealing potential as a result of shear with temperature (SSP_{τ}). However, the spread in the data is much greater than seen in SSP_{H2O}. Even considering the spread of data, the data do suggest that self-sealing potential by shear also reduces with temperature.

In conclusion, for Opalinus Clay, this SSP indicator indicates that the effectiveness of self-sealing processes reduces at elevated temperatures.

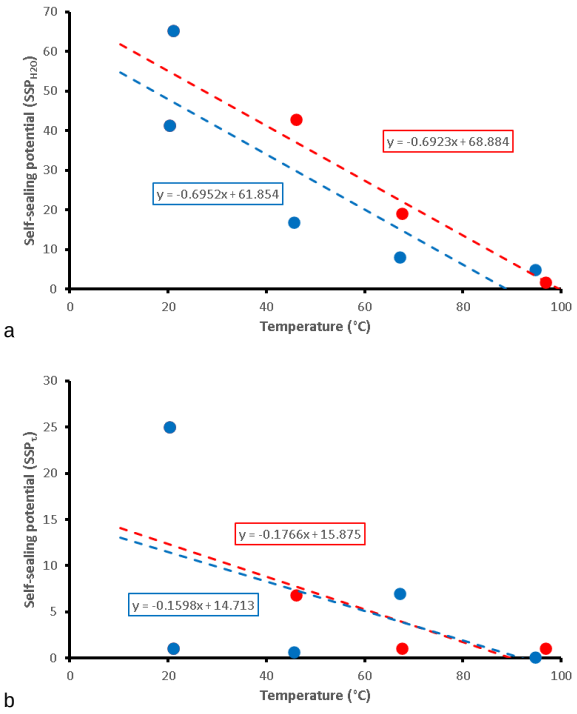

Figure 2-20 – Influence of temperature on self-sealing potential. a) Self-sealing potential as a result of hydration; b) Self-sealing potential as a result of active shear. The blue circles show the data for fractures that were initially fractured at ambient temperature, while the red circles show the data that were initially sheared, and subsequently re-sheared, at elevated temperature

The dataset for Callovo-Oxfordian claystone is incomplete at the time of reporting. However, four tests were completed at the four test temperatures in order to make preliminary statements about the role of temperature on self-sealing in Callovo-Oxfordian claystone.

Figure 2-21 shows the result for self-sealing potential for Callovo-Oxfordian claystone. As shown, the HITEC self-sealing potential because of water (SSP_{H2O}) reduces in Cox with increased temperature (Figure 2-21a). This is a marked reduction, with SSP_{H2O} of 132 at 20 °C, reducing to 7 at 90 °C. That is nearly a two order in magnitude reduction in the effectiveness of self-sealing as a result of water flow. Therefore, at elevated temperatures the fractures are less likely to self-seal. Figure 2-21b also shows a reduction in self-sealing potential as a result of shear (SSP_{τ}). It must be noted that the spread in data is considerable and as a result is not yet clear whether this reduction is a considerable one, or a moderate one. The preliminary data for Callovo-Oxfordian claystone suggest that the favourable self-sealing properties of the rock reduce with temperature.

Two of the four tests conducted in Callovo-Oxfordian claystone need repeating because of problems encountered during repeat shearing. In addition, another four tests are required to describe the self-sealing properties for fractures formed at ambient temperatures. These additional six tests will expand the dataset and allow clearer statements to be made on the role temperature plays on shear properties and self-sealing potential in Callovo-Oxfordian claystone.

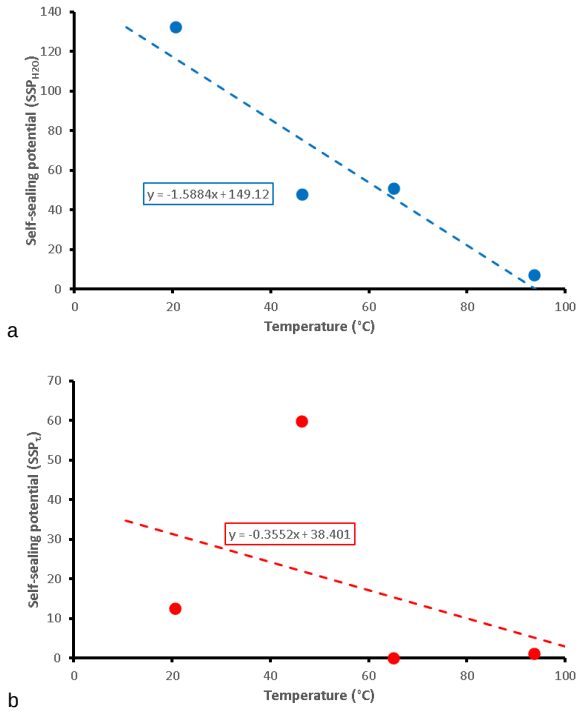

Figure 2-21 – Influence of temperature on self-sealing potential in Callovo-Oxfordian claystone. a) Self-sealing potential as a result of hydration; b) Self-sealing potential as a result of active shear. The blue circles show the data for fractures that were initially fractured at ambient temperature, while the red circles show the data that were initially sheared, and subsequently re-sheared, at elevated temperature

2.3.2.3 Conclusion

Previous experiments of fracture flow have concentrated on the transmissivity of water. These experiments have shown that water flow along a fracture can reduce fracture transmissivity by up to one order of magnitude. Active shear of the fracture can result in a further order of magnitude reduction in flow, although prolonged flow can result in increases of transmissivity. This had been interpretated as showing hydraulic flow and shear are effective self-sealing mechanisms in clay-rich rocks. This was assumed to also apply to gas flow. The current study has shown that the assumption that hydration and shear are effective self-sealing mechanism for gas flow may be over simplified.

Considerable variation was noted in initial gas flow for all three rock types tested. No systematic correlation was found between fracture properties (roughness, peak to valley height etc) and initial gas (or water) flow properties. This has been attributed to fracture roughness not being a direct proxy for

fracture mismatch, with the latter being a measure of asperities within the fracture plane that are conductive to gas.

This study has defined a new parameter, called Self-Sealing Potential (SSP), to remove the variation in flow rates seen. In the GAS WP, self-Sealing Potential as a result of hydration (SSP_{H2O}) is a measure of the proportional change in gas flow seen before and after hydraulic flow along the fracture. Self-Sealing Potential as a result of shear (SSP_{τ}) is a measure of the proportional change in gas flow as a result of active shear movement. For both parameters, SSP > 1 indicates a decrease in flow, SSP < 1 indicating an increase in flow. For most scenarios in radioactive flow, SSP > 1 is preferrable. The current study suggests that 0.9 < SSP < 1.25 means that no change in flow has been seen, although this could be extended to 0.8 < SSP < 1.5 to include only minor changes in self-sealing.

This SSP parameter suggests that neither hydration nor shear were effective self-sealing processes for gas flow in the Boom Clay. It was concluded that both hydration and shear resulted in small increases in gas flow in Boom Clay or no change in flow properties. Data suggested that excess water on the fracture plane resulted in increased gas flow. At the two stress conditions investigated, both showed the same self-sealing potential result because of shear. In response to hydration, discounting one sample that showed considerable sealing, no test showed a significant change in flow. However, the data suggests at the lower stress condition flow increased, whereas at the higher stress condition flow decreased. A rougher fracture was seen to have a better self-sealing potential (SSP_{H2O}) as it will result in greater surface area being accessed by water for swelling. However, a smoother fracture resulted in more enhanced gas flow and a smaller SSP_{τ}.

For the other two rocks, a considerable difference is seen in the self-sealing potential of hydration and shear. Hydration was seen to decrease gas flow in both the Callovo-Oxfordian claystone and Opalinus Clay, with an average reduction of over two orders of magnitude in the latter for perpendicular shearing. However, as a result of shear, both Callovo-Oxfordian claystone and Opalinus Clay saw an increase in flow. In Cox, an increase in roughness reduces the effectiveness of hydraulic self-sealing, as rough fractures have considerable mismatch between the two faces of the fracture. A strong trend was seen between average roughness and SSP_{τ}. Therefore, a smoother fracture results in greater enhanced flow. This will be related to mismatch between the two surfaces of the fracture. On the other hand, in OPA, a positive relationship was seen between SSP_{H2O} and average roughness, and a negative relationship between SSP_{τ} and average roughness. Therefore, a rougher fracture results in a better gas seal following hydration, but a worse seal because of shear.

Generally, no variation was seen in Callovo-Oxfordian claystone with respect to shear direction (perpendicular and parallel to bedding), but a systematic difference was observed in Opalinus Clay: shear was seen to enhance gas flow, with a small increase when sheared parallel to bedding and a significant increase perpendicular to bedding.

At the time of reporting, a total of 13 of at least 21 shear experiments had been completed in the HITEC WP. The experimental programme was late to start because of the Covid-19 pandemic and delays to the modification of the apparatus. All planned experiments in Opalinus Clay had been completed, with enough experiments in Callovo-Oxfordian claystone to make statements about the influence of temperature on shear properties and flow. None of the experiments using Boom Clay had been conducted.

The preliminary results indicate that the self-sealing potential changes with temperature in both Opalinus Clay and Callovo-Oxfordian claystone. A clear relationship was seen with SSP_{H2O}, with a reduction in self-sealing capacity with increasing temperature for both rocks. At a temperature of 90 °C, the self-sealing potential was negligible. A difference was seen between SSP_{H2O} for fractures that were formed at ambient temperature and those formed at temperature, although this may simply be explained by natural variation between samples. This result suggests that SSP_{H2O} is better in fractures that have formed at temperature. This may be related to differences in fracture topology. A reduction was also

seen in the effectiveness of self-sealing because of active shear (SSP_{τ}), although the reduction was not as marked as for water and the data showed considerable spread.

All fracture surfaces were laser scanned following the initial and re-shear stages of the experiment, giving four fracture topology scans per test. Little variation was seen in roughness characteristics for the initial shear samples, with a reduction in roughness seen during re-shear. For peak to valley height, an increase was seen with temperature for the initial shear samples, with a reduction seen for the re-shear tests. All three datasets suggest that little variation is seen in fracture topology for shear fractures created at different temperatures in initially intact samples. The presence of water during the re-shear phase results in the reduction in fracture roughness and peak to valley height. As self-sealing potential (SSP_{H2O}) is a function of temperature, and fracture roughness alters with temperature, it is likely that fracture roughness plays a role in the effectiveness of fractures to self-seal.

2.3.3 UGrenoble (CNRS) - Self-sealing tests in oedometric cell

2.3.3.1 Introduction

Fractures subject to water circulation in some clayey rocks can fully or partially close, leading to a self-sealing process. The swelling phenomena of the material around the lips of the crack are sensitive to water re-saturation, they could also be sensitive to temperature. The experiments that have been conducted tended to make it possible to characterise both the swelling (volume deformation) of the material in the vicinity of the fault, as well as the evolution of the water content, at different temperature levels and with two orientations of the fault with respect to the bedding of the rock.

The material is the Callovo-Oxfordian clay rock, which comes from the clay unit of the Meuse/Haute Marne research underground laboratory (URL) in France. All the samples were cut from the same core EST62674 with a carbonate content of approximately 20.5%. The initial water content was 6.7%.

2.3.3.2 Experimental devices and procedures

The fracture sealing tests were performed in an in-house cell that was developed initially for our laboratory x-ray tomograph. The device has been adapted to be used on the D50 beamline from ILL for dual x-ray and neutron tomography and with a temperature control up to 90°C (Figure 1).

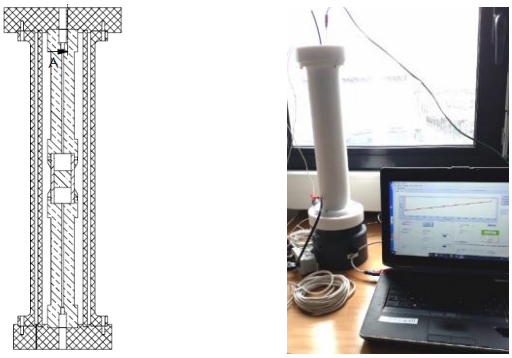

Figure 2-22 – Schematic and photograph of the cell developed for tests with dual x-ray and neutron CT

A preliminary analysis was conducted to exploit the data from the bi-modal x-ray and neutron tomography. Radiation absorption depends on both the mass density of the solid phase and the mass density of the aqueous phase (free water and confined water). During a swelling process, these respective densities evolve, leading to an evolution of the absorption levels. In addition, the kinematic

field (strain tensor) can be calculated from tomography images (mainly x-ray CT) by a digital image correlation (DIC) method. The link between volume strain and absorption level, subject to a few assumptions, also involves the variation in the saturation level of the rock. This theoretical analysis was compared to previous experimental results and shows a relatively good predictive character (Stavropoulou et al., 2020).

Sealing tests at different temperatures were then performed at D50 beamline. Due to a limited time access to the large facility, time duration of each test was limited to a few hours, allowing characterising the short-term sealing process.

2.3.3.3 Research plan

Cylindrical specimens (centimetric size) were cut from in-situ collected cores and prepared with a synthetic crack in the middle axial plane. The crack was initially open and the specimen placed in oedometric conditions (no radial displacement of the outer boundary). Neutron and x-ray scans were done during the flow of synthetic host pore water (site salinity) through the crack every 15 minutes. Crack closure, local swelling around crack and water re-saturation (water content evolution) were quantified thanks to neutron and x-ray scans and DIC analysis. Tests were performed at three different temperatures to observe an eventual thermal impact on the sealing process. Because sealing can be also affected by material anisotropy, some specimens have been sampled parallel to the bedding, others perpendicular. A total of 6 tests were performed, as described in Table 2-10.

Table 2-10 – Experimental program of self-sealing characterization

Tests	Temperature (°C)	Orientation/bedding
1	25	//
2	60	//
3	90	//
4	25	⊥
5	60	⊥
6	90	⊥

2.3.3.4 Results and discussion

X-ray and neutron scans were taken for each of the six tests, with a voxel size of 35 µm for x-ray CT and 70 µm for neutron CT. These images have neither the same spatial resolution (number of voxels), nor the same coordinate system, so they had to be realigned to enable image pairs to be compared. The x-ray images were of good quality, but the neutron tomography images were unexpectedly noisy when water was injected into the crack, most likely due to a diffraction phenomenon induced by the presence of the hydrogen in the water. This loud noise, which could not be corrected during the experimental campaign, severely hampered the possibility of the detailed analysis that was planned. Processing was carried out to extract information from these noisy images, but it was much coarser than originally envisaged.

We compare here the results of two tests with the crack parallel to the bedding at 25°C and 90°C. For the 90°C case, the scans were taken when the sample was at 90°C (heating prior to placement on the imaging platform), before and after water injection, in order to monitor the sample over time.

Figure 2-23 and *Figure 2-24* show vertical sections of the x-ray scans for the two tests. At 25°C, the scans show a fairly rapid closure of the interface by the formation of a zone with a thickness of about twice the initial opening of the interface and where the level of x-ray absorption falls. This zone fills the interface almost instantaneously. This mechanism has already been observed at room temperature and

is the site of multiple cracks sub-parallel to the bedding, which forms a very damaged material (Di Donna et al., 2022).

For the test at 90°C, a gradual reclosure of the interface can be seen during the first three hours, as well as the formation of a few secondary cracks sub-parallel to the interface. The presence of these secondary cracks seems to be partly influenced by the presence of large pyrite inclusions, visible on the tomographic cross-sections. On *Figure 2-24*, the lower part of the sample closes more quickly, probably due to secondary cracks in this zone, unlike the upper part. The total volume of the interface disappeared around three hours (*Figure 2-25*b). At the end of almost 7 hours of observation, the crack gives the appearance of having closed, with a level of x-ray absorption in the interface that has largely increased, even if it does not reach the level of the intact material (*Figure 2-26*b).

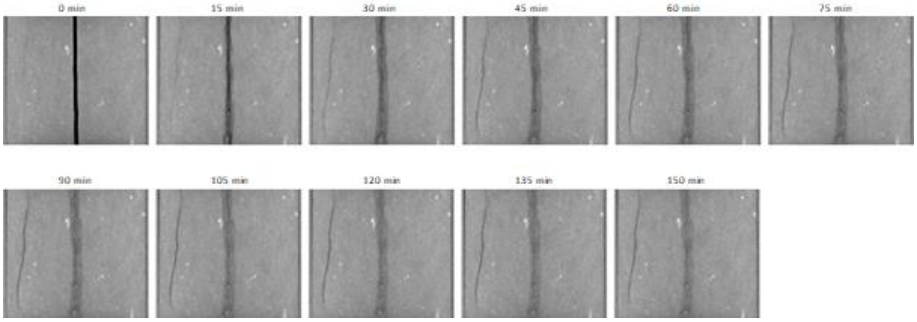

Figure 2-23 – Test at 25°C, time evolution of a vertical x-ray tomographic section

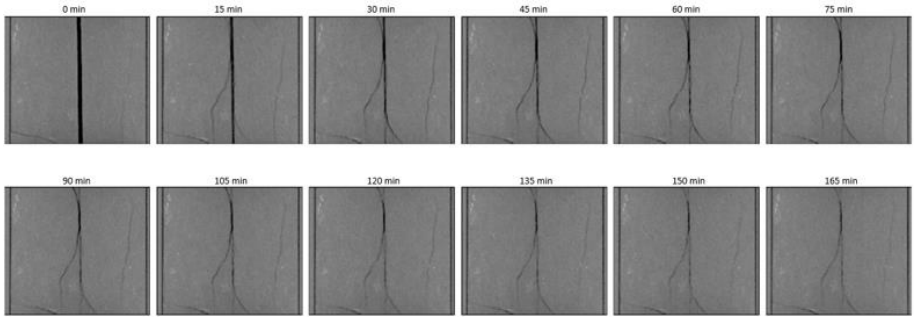

Figure 2-24 – Test at 90°C, time evolution of a vertical x-ray tomographic section

If one considers the evolution of the overall volume of the interface (*Figure 2-25*), the kinetics of complete reclosure are of the order of 3 hours and the levels of x-ray absorption reached at the end of these three hours (*Figure 2-26*) are comparable to those observed at 90°C.

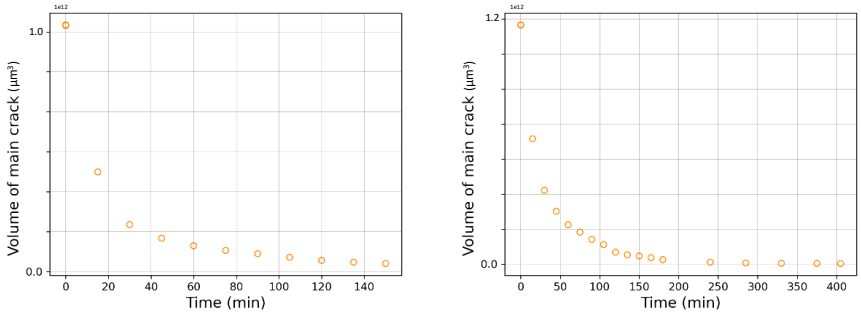

(a) *(b)*

Figure 2-25 – Evolution with time of the interface volume – (a) test at 25°C and (b) at 90°C

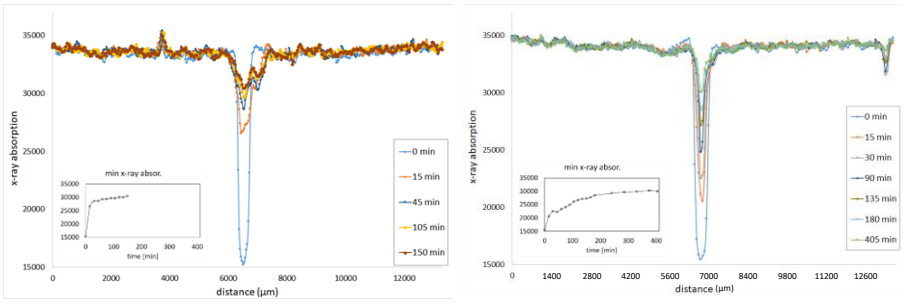

(a) *(b)*

Figure 2-26 – profiles of x-ray absorption across the interface and (small) evolution with time of the minimum if x-ray absorption in the interface – (a) test at 25°C and (b) at 90°C

The neutron tomography images show a zone of high water content in the interface. In *Figure 2-27*, the zone appears wider and more pronounced at 25°C than in the 90°C test. This corroborates the x-ray CT observations. The central zone of intense cracking absorbs a large amount of water.

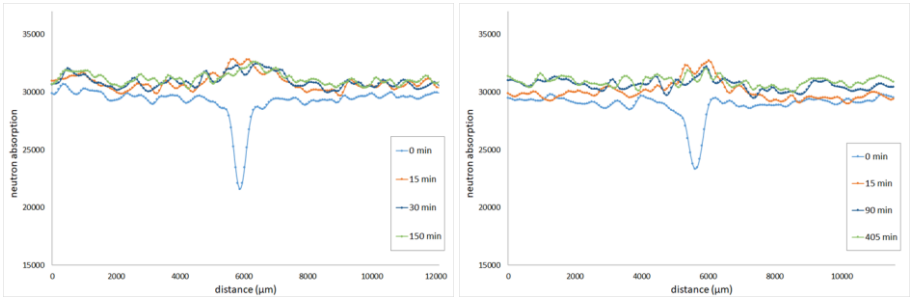

Figure 2-27 – Profiles of neutron absorption across the interface – test at 25°C and at 90°C

2.3.3.5 Conclusion

It should be remembered that the fracture closure process is considered over a very short period, which cannot predict the phenomena and kinetics over longer periods.

If we compare the phenomena at 90°C and 25°C, the reclosure mechanism is not fully identical. At low temperatures, quasi-instantaneous closure is favoured by the formation of a dense network of micro-cracks sub-parallel to the bedding in the area close to the interface lips, creating a highly damaged material that fills the interface space. **At 90°C, the mechanism is more diffuse and any secondary cracks are scattered. The reclosure kinetics are more gradual and are favoured by a diffuse swelling in the whole sample, much greater in intensity than at 25°C.** In both cases, the interface with an initial opening of around 0.3 mm was completely filled within around 3 hours, although the mechanisms were slightly different, showing a more ductile character at 90°C.

A better understanding of the self-sealing mechanism would require the ability to quantify and compare changes in water content and volume deformation. This comparison would provide a better understanding of whether the degree of saturation of the material changes during self-sealing. The quality of the neutron tomographic images needs to be improved, which could not be done in this study due to the very restrictive access conditions to the large facility. Stress conditions should also be introduced to recreate in situ conditions and analyse an eventual stress effect. Finally, a measurement of the hydraulic conductivity of the interface during self-sealing would enable the quality of the sealing to be quantified.

2.3.4 GRS - Experimental study of gas transport and impact on self-sealing of fractures in indurated claystone

In this study, self-sealing of fractures in the Callovo-Oxfordian (Cox) and Opalinus (OPA) claystones, was investigated on artificially fractured samples. The samples were extracted from four lithological facies relatively rich in clay mineral, carbonate and quartz, respectively. Long-term consolidation, water and gas flow experiments were undertaken on the fractured samples with different sizes and fracture intensities. The self-sealing of fractures was measured by fracture closure, water permeability variation, gas penetration, and recovery of gas-induced pathways.

Most of the fractured samples exhibited a reduction in water permeability to levels close to that of intact rock. It has been observed that self-sealing efficiently depends on the mineral composition of the sample with higher capacity for the clay-rich samples than for the carbonate-rich and sandy ones. Gas breakthrough pressures in the sealed fractures are lower than the one measured on intact rocks and still lower than the confining stresses. The gas-induced pathways can recover when contacting water. These important findings imply that fractures in such indurated claystone can effectively recover to hinder water transport but allow gas release without compromising the rock integrity.

2.3.4.1 Description of the tests and experimental set up

Two GRS designed setups were used for self-sealing tests on the fractured claystone samples. Figure 2-28 and Figure 2-29 illustrate the schematic assemblies of both setups. The first setup (Figure 2-28) consists of three triaxial cells and three samples can be tested simultaneously under identical conditions. The triaxial cells allow cylindrical samples of a diameter of 50 mm and different lengths of 70-120 mm.

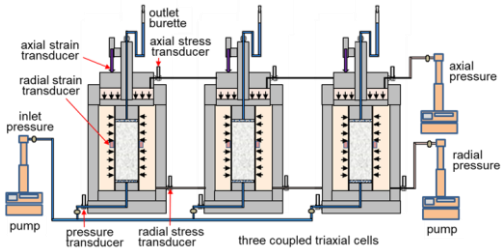

Figure 2-28 – Setups for testing of water and gas transport in fractured claystone samples under identical hydro-mechanical conditions: A setup with three triaxial cells for hydro-mechanical testing of three samples in parallel.

The second set up were tested in a pressure vessel (Figure 2-29), which allows hydraulic testing of four samples in parallel under identical conditions. Large samples can be used in this set up with diameters about 80 mm and length up to 300mm.

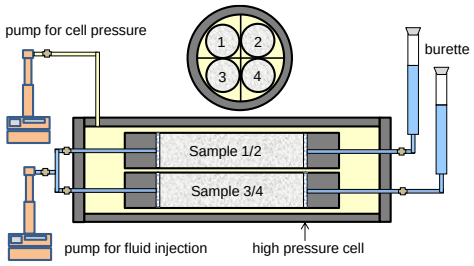

Figure 2-29 Setups for testing of water and gas transport in 4 fractured claystone samples under identical hydro-mechanical conditions: A pressure vessel for hydraulic testing of four samples in parallel

The samples were fractured following Brazilian test technics generating tensile fracture in the clay rock. The cylindrical specimen of rock is loaded in a diametrical plane along its axis (see Figure 2-30a). In one of the samples, a regular fracture was produced in a half-part by milling to a width of 30 mm and an aperture opening of 2 mm at the middle along the length (see Figure 2-30f).

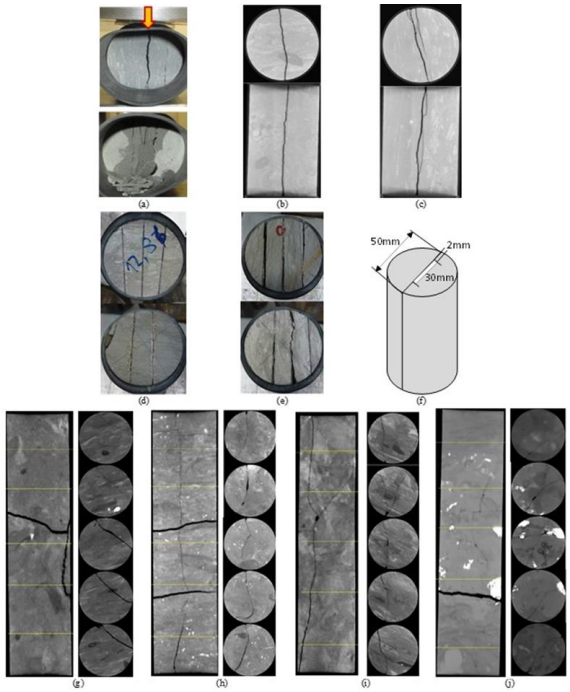

Figure 2-30 – Fracture patterns in the claystone samples illustrated with photos: (a) COX1, (b) COX3, and (c) OPA1; (d) OPA2, (e) OPA3, and (f) OPA4; (g) COX2 (D/L = 80/298 mm), (h) COX4 (D/L = 80/283 mm), (i) COX5 (D/L = 80/300 mm), and (j) COX6 (D/L = 80/280 mm).

Four samples were taken from OPA sandy facies, two from Cox clay-rich and four from Cox carbonate-rich. They were prepared to different sizes of diameter / length (D/L) = 50 / (75-100) and 79 / (280-300) in mm. Their characteristics determined before testing are summarized in Table 2-11. All the OPA and Cox samples have similar solid grain densities of 2.69 – 2.70 g/cm^3 (Zhang et al. 2019; Zhang and Laurich, 2020). The OPA sandy samples have relatively high dry densities or lower porosities compared to the Cox carbonate- and clay-rich samples. The physical properties of each facies vary from a sample to another, indicating the heterogeneity of the clay facies, particularly the OPA sandy and Cox carbonate-rich facies. Due to sampling and long storage durations of 1-2 years, the samples were desaturated to 43-50% degrees at OPA samples, ~70% degree at Cox clay-rich ones and 27-54% at Cox carbonate-rich ones.

Table 2-11 – Initial characteristics of the claystone samples before testing.

a mis en forme : Normal

Lithological facies	Drilled core	Depth/ orientation	Sample number	Size D/L (mm)	Bulk density (g/cm^3)	Dry density (g/cm^3)	Poro-sity (%)	Water content (%)	Degree of saturation (%)
OPA sandy facies	BLT-A10		OPA1	50/75	2.487	2.445	9.4	1.72	44
	BDM-B9-9		OPA2	50/90	2.515	2.478	8.2	1.49	45
	DBM-B9-18		OPA3	50/90	2.563	2.532	6.2	1.22	50
	DBM-B9-29		OPA4	50/90	2.559	2.527	6.4	1.27	50
Cox clay-rich unit (UA)	EST49093	-482m/V	COX1	50/100	2.383	2.262	16.2	5.35	75

Cox transition unit (UT)	EST57262	-456m/V	COX2	80/298	2.400	2.291	15.1	4.76	72
Cox carbonate-rich unit (USC)	EST51223	-444m/H	COX3	50/80	2.437	2.369	12.2	2.87	56
	EST52318	-437m/V	COX4	80/283	2.584	2.553	5.4	1.21	56
	EST52335	-445m/H	COX5	80/300	2.425	2.397	11.2	1.14	25
	EST52337	-445m/H	COX6	80/280	2.434	2.405	10.9	1.21	27

A general test procedure was performed on the fractured claystone samples in each group in three phases:

i. **Self-sealing:** The self-sealing of fractures created in the samples was measured by water permeability and fracture closure under confining stresses. Synthetic Cox and OPA water were injected to the respective Cox and OPA samples. The confining stress was stepwise increased during which the synthetic water was continuously injected to the samples at pressures of 0.1 – 1.0 MPa. Each load step lasted for a long period of 1 – 4 months. During steady-state water flow, apparent water permeability has been determined.

ii. **Gas testing:** Following the water flow at the last load step, gas penetration testing was then undertaken. Helium gas was injected into the inlet by stepwise increasing pressure with small increments of 0.1 – 0.2 MPa at time intervals of 1 – 3 days. As first gas bubbles were detected at the outlet side at atmospheric pressure, the gas pressure in the inlet was considered as the gas breakthrough pressure Pb. Beyond the breakthrough, the gas injection continued for determination of apparent gas permeability.

iii. **Resealing**: In order to examine resealing capacity of gas-induced pathways, synthetic porewater was reinjected to the samples again. Water permeabilities before and after the gas flow were compared to highlight the gas impact on the self-sealing of fractures in the claystones.

iv. **Post-testing:** The samples was loaded down and dismantled. They were then confined in the rubber jackets and fixed in PVC tubes. The confined samples were scanned by μ-CT for visualization of the resealed fractures.

2.3.4.2 Experimental results

As a key parameter of fracture sealing, the water permeability of each fractured sample was measured during water injection under increased stresses. The results are depicted for selected samples in Figure 2-31.

Initially, the permeabilities of fractured samples were determined by gas injection at a pressure of 0.03 MPa and under the low stresses of 1 and 2 MPa. High gas permeabilities were obtained (10^{-13}–10^{-12} m^2) for all samples. As soon as the water was supplied, the fracture walls were wetted and expanded into the interstices and clogged the pathways. This significantly decreased the permeability by several orders of magnitude to low values of 10^{-18}–10^{-17} m^2 at the clay-rich facies of COX1 and COX2, 10^{-16}–10^{-14} m^2 at the sandy ones of OPA1-4, and 10^{-15}–10^{-13} m^2 at the carbonate-rich ones of COX3-6. The permeability reduction continued with time to lower values of 10^{-18}–10^{-17} m^2 within 1-2 months for most samples. However, the carbonate-rich sample COX3 with a low clay content of 21% and two sandy ones OPA3 and OPA4 with high fracture intensities exhibited a limited permeability reduction to 10^{-15}–10^{-14} m^2 (see for example, Figure 2-31). Furthermore, by comparing the results from the different samples, more effects can be identified as follows.

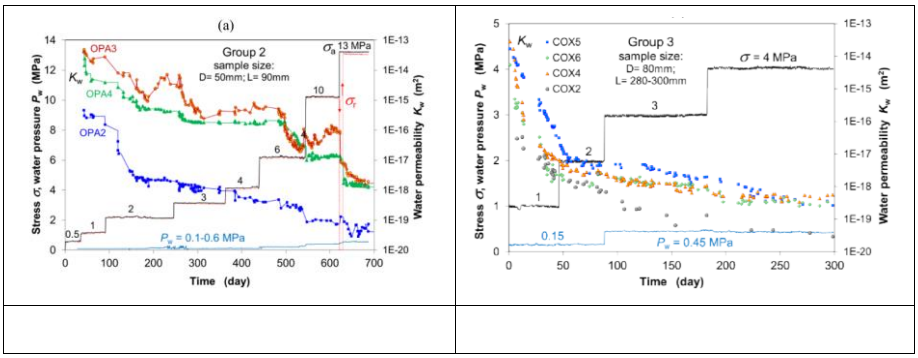

Figure 2-31 Example of evolution of the water permeability measured on the fractured Cox and OPA claystones during water injection under increased confining stresses.

2.3.4.2.1 Effect of mineralogical composition

The fracture sealing is determined mainly by the swelling capacity of the claystone, which is in turn determined by its clay content. The higher the clay content, the more water it can absorb, leading to more swelling and slaking of the fracture walls and clogging the interstices more effectively.

2.3.4.2.2 Effect of fracture ~~intensity~~network characteristics

The OPA sandy samples had been fractured to different geometries or intensities. The water permeabilities of samples OPA3 with three parallel fractures and OPA4 with a wide aperture of 2 mm are 2-3 orders higher than those of the relatively less fractured ones, i.e., OPA1 with a single fracture and OPA2 with three, but one inclined to a dead end. This illustrates the significance of fracture network characteristics ~~intensit~~y (density, aperture, connectivity, etc.) for the fracture permeability, particularly for the initial value. With water flow, the initial sharp fracture patterns tend to disappear to mud with more homogeneously redistributed micropores. Further variation of the permeability with load is then more dominated by the consolidation of the mud and the stiffness of the surrounding claystone matrix.

2.3.4.2.3 Scale effect

A scale effect can be recognised by comparing the water permeabilities of the large samples COX4-6 with lengths (L) of 280-300 mm and the small one COX3 with L = 80 mm from the same borehole in the carbonate-rich unit. The large samples, even though more intensively fractured, showed low Kw values of approximately 3×10^{-19} m² at a stress of 4 MPa, being four orders of magnitude lower than that of the small sample even at high stress up to 10 MPa. As mentioned earlier, the distribution of carbonates is heterogeneous, and appears in the form of bands on centimetre- to decimetre-scale. If a fracture network is distributed through both carbonate-rich and clay-rich regions, the self-sealing performance of the entire network is determined mainly by the clay-rich part of the network.

2.3.4.2.4 Stress dependence of fracture sealing

Two key parameters of the fracture sealing, i.e., fracture closure (or compaction) and water permeability, are strongly dependent on the applied stress. The Kw data are summarised in Figure 2-32 as a function of the effective stress for most samples including the previous results from the clay-rich samples COX7-10 (Zhang, 2013). A dependence of water permeability on effective stress and on the clay content can be seen on this figure. The slope of the $\log_{10} K_w$–σ_{eff} curve varies with mineralogical composition.

Generally, the test results from the representative samples showed significant self-sealing of fractures in the clay-, carbonate- and sand-rich claystones. Most of the fractured samples reached low water permeabilities of 10^{-18}-10^{-20} m² even at relative low stresses of 2-4 MPa. These values are relatively close to that of the intact claystone. By extrapolation of the test data to the in situ conditions, a complete

recovery of the EDZ can be expected during a long-term consolidation phase of tens of thousands of years. This important conclusion needs to be further confirmed with in situ tests performed in the EDZ.

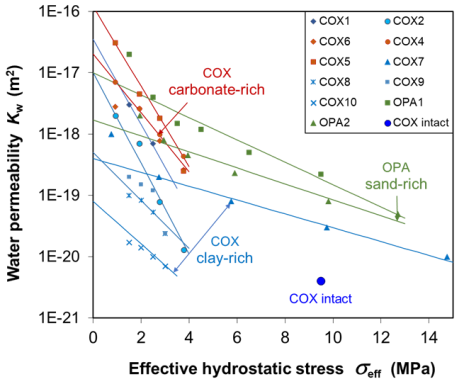

Figure 2-32 – Water permeabilities of the fractured claystone samples as a function of effective hydrostatic stress (blue colour for clay-rich Cox, red for carbonate-rich Cox, green for sandy OPA).

2.3.4.2.5 Gas penetration and impact

Gas testing followed the last consolidation stage to investigate gas penetration through sealed fractures and recovery of gas-induced pathways. Results are illustrated in Figure 2-33.

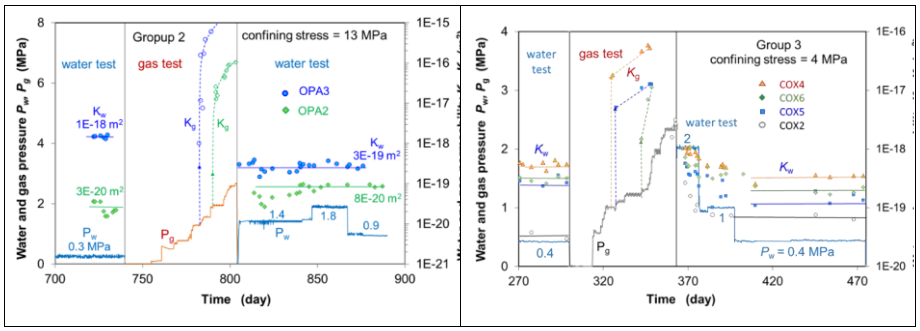

Figure 2-33 – Gas breakthrough pressures and permeability variations of the samples and resealing of gas pathways by water flow

The measured gas breakthrough pressures are summarised in Table 2-12. The gas breakthrough pressure depends on the sealing ~~intensity~~ efficienty of the fractures, which can be represented by the water permeability. Theoretical studies and experimental measurements on rock samples in laboratory and in different rocks, such as plastic clay, indurated shale, limestone, anhydrite, and bedded salt (Volckaert et al., 1995; Horseman et al., 1996; Rodwell et al., 1999), suggest also that gas breakthrough pressure is dependent on water permeability. The gas breakthrough pressure is also related to the minimum principal stress σ_{min}.

All the gas breakthrough pressures observed do not reach the gas fracturing threshold pressure P_{fr} of the rocks:

$$P_b < P_{fr} = \sigma_{min} + \sigma_T$$

where σ_T is the tensile strength of 1–2 MPa for the intact claystones OPA and Cox (Bock et al., 2010). Because the gas breakthrough pressures of the sealed claystones are always lower than the intact ones, the EDZ, even when highly sealed, can still act as preferable pathways for gas release without compromising the integrity and barrier functions of the host Cox and OPA formations.

Table 2-12 – Results of measured gas breakthrough pressure Pb, water permeability before (K_{wa}) and after (K_{wb}) gas penetration through the resealed claystone samples under various confining stresses σ.

Group No.	Sample	σ (MPa)	P_b (MPa)	K_{wa} (m^2)	K_{wb} (m^2)
1	COX3	10	1.1	2×10^{-15}	-
	OPA1	10	5.5	2×10^{-19}	-
2	OPA2	13	2	3×10^{-20}	8×10^{-20}
	OPA3	13	1.3	1×10^{-18}	3×10^{-19}
3	COX2	4	2.3	3×10^{-20}	6×10^{-20}
	COX4	4	1	6×10^{-19}	3×10^{-19}
	COX5	4	1.1	3×10^{-19}	1×10^{-19}
	COX6	4	1.2	3×10^{-19}	2×10^{-19}

Gas-induced pathway recovery was examined by measuring water permeability and comparing it with that prior to gas penetration. All samples exhibited low values of K_w. Most samples showed some reduction of water permeability after gas penetration than before. Generally, the results indicate a significant recovery of gas-induced pathways in the studied claystones.

2.3.4.2.6 Long-term gas migration

In order to understand long-term gas migration through the resealed pathways, gas was injected simultaneously into the resealed gas pathways in the four large samples COX2 and COX4-6 for longer time periods (about 2 months). Figure 2-34 show the evolution of the inlet gas pressure and outflow rates of the samples as “a whole resealed EDZ” during gas injection phase. The confining stress was kept at 4 MPa.

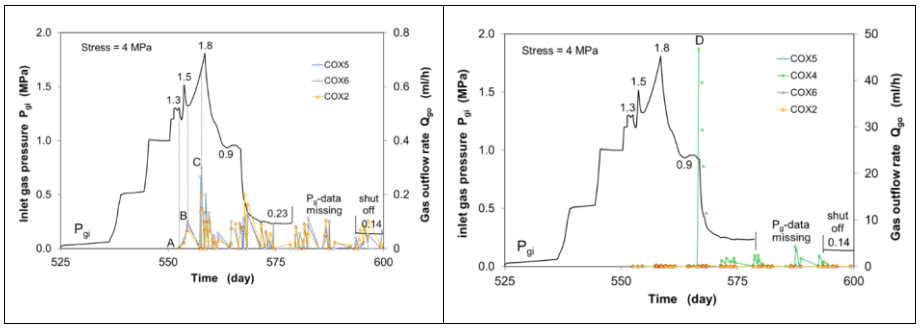

Figure 2-34 – Long-term evolution of the inlet gas pressure and outflow rates obtained on the fractured resealed Cox samples during the first phase.

The tests indicate that the advective movement of gas through the resealed samples varies temporally and spatially, reflecting unstable pathways with multiple opening/sealing processes. The question if a steady gas flow will be reached over the much longer time periods and repository conditions, still needs to be answered in the future.

2.3.4.3 Conclusion

The self-sealing of fractures was measured by fracture closure, water permeability, and gas breakthrough pressure. Influence of mineralogical composition, sample size, fracture network characteristics, water or gas injection pressure, and confining stress was studied. The studied Cox and OPA claystones with the different mineralogical compositions and properties have shown favourable self-sealing capacities for the long-term isolation of radioactive waste. Under combined impact of mechanical compression and clay swelling, the fractures tend to seal to low water permeabilities of 10^{-18} – 10^{-20} m^2 being close to that of the intact rock for both clay rocks (Levasseur et al, 2021). The fracture sealing efficiency that is characterised by water permeability is dependent on the mineralogical composition, initial fracture network characteristics, effective confining stress, and load duration. The self-sealing capacity of the clay-rich claystone is higher than that of the carbonate-rich and sandy ones. A significant scale effect is observed due to the heterogeneous distribution of the mineralogical components, particularly clay minerals.

Based on the test data obtained on the fracture-sealed and intact samples, it has been shown that gas breakthrough pressure depends on the fracture sealing efficiency (water permeability) and the effective confining stress. The gas breakthrough pressures of the sealed fractures are lower than that of the intact samples. This suggests that the EDZ, even highly consolidated, can still act a preferable path for gas release without compromising the integrity of the host rock. All the gas breakthrough pressures observed are lower than the applied confining stresses. The gas flow process recorded varies temporally and spatially, reflecting unstable pathways with multiple opening/sealing cycles. When water is injected again, the gas-induced pathways tend to reseal.

2.3.5 EPFL - Gas transport in intact and remoulded/recompacted claystone

EPFL's experimental program on Opalinus Clay addresses two major aspects, namely (i) the phenomena and processes related to the initiation and propagation of rock failure in response to gas pressure build-up, and (ii) the phenomena and processes that contribute to the self-sealing of OPA after gas invasion. The proposed experiments are combined water/gas injection experiments with an oedometer cell, allowing for assessment of axial strain.

2.3.5.1 Description of experimental set up

The experimental work used a high-pressure oedometer cell specifically developed to analyse the hydro mechanical behaviour of geomaterials at high-confining stresses (Ferrari et al., 2013). The layout of the apparatus is depicted in Figure 2-35. The cell is designed to hold cylindrical specimens with a height and diameter of 12 mm and 35 mm, respectively. The specimens are placed in a stainless steel oedometer ring with a thickness of 15 mm. The bottom and top parts of the specimen in the oedometric ring are in contact with metallic plates equipped with a drainage system. The latter is composed of vertical holes which are connected by a spiral path. The spiral path is then connected to the water/gas injection systems as shown in Figure 2-36. Pre-compressed filter paper disks are placed between the specimen and the plates. The interfaces between each element are sealed using O-rings.

The vertical load is applied by a hydraulic jack connected to a volume/pressure controller (VPC), enabling it to reach a vertical total stress up to 100 MPa. Different VPCs can be connected to the oedometer cell to perform water and gas injections from the bottom and top side of the specimen with a fluid pressure up to 16 MPa (water) and 20 MPa (gas). The assessment of the vertical deformation was done using three Linear Variable Differential Transformers (LVDTs) which measure the relative displacement of the cell with respect to the piston. The natural specimens were tested with the vertical mechanical load and fluid injection perpendicular to bedding plane (S sample).

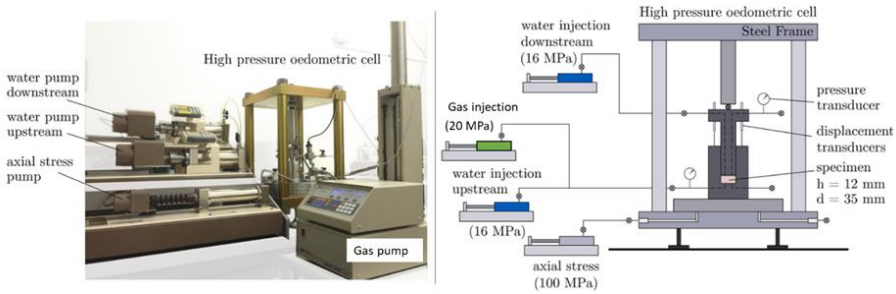

Figure 2-35 – High pressure oedometer test set-up.

Figure 2-36 – Oedometer ring with the metallic base

For the oedometric and hydraulic conductivity tests on natural OPA, synthetic porewater was used in order to reproduce the chemical composition of the in situ porewater, which may affect the hydro mechanical response of clayey geomaterials.

The core samples used in this experimental campaign were retrieved from the deep borehole in Trüllikon (TRU1-1) in the Zürich Northeast siting region in Switzerland (Ammen and Palten, 2021) and were sourced from a depth of about 850 m. A complete geotechnical characterization has been performed on the tested specimens, as shown in Table 2-13 (natural OPA).

Table 2-13 – Material properties of tested specimens – Natural OPA; GW = gas/water injection tests,.

Material	OPA_848
Test	GW
Depth (m)	848.7
Bulk density, ρ *(g/cm³)*	2.50
Density of solid particles, ρ_s (g/cm³)	2.78
Void ratio, e (-)	0.15

Degree of saturation, *Sr* (-)	0.63
Initial total suction, ψ (MPa)	66

First, the location of the specimen was selected on the core sample using X-ray images to prevent from choosing initially cracked or heterogeneous portions. A slice with a thickness of approximately 30 mm was sawn from the core without unpacking it, in order to minimize the disturbance to the specimen. For the water/gas injection test in the oedometer apparatus, a cylinder with a diameter slightly larger than the final confining ring was obtained using a lathe machine; final re-coring was performed using a hydraulic press. Lastly, the lower and upper faces were smoothed using sandpaper in order to obtain parallel and plane surfaces. No fluid was used during the specimen preparation phase in order to preserve the original water content/composition as much as possible and to reduce the disturbance of the material due to swelling.

2.3.5.2 Injection tests on natural OPA

The test started first with a water resaturation in isovolumetric conditions using synthetic water mimicking the in-situ porewater. This protocol was followed to preserve the quality of the specimen and assure that it was not significantly affected by the saturation phase. Once the deformation and water uptake were stabilized, the saturation phase was considered complete and the total vertical stress corresponds to the swelling pressure.

Once the resaturation (sequence (i) in Figure 2-37) was achieved, (ii) a mechanical loading up to the target vertical effective stress was performed to simulate in-situ stress conditions. To do so, constant water pressure at the bottom ($u_{w,bot}$) and top ($u_{w,top}$) of the specimen was applied ($u_{w,bot} = u_{w,top} = 1$ MPa) and the vertical total stress σ_v was increased in steps up to σ_v = 15 MPa. (iii) Constant head water permeability tests were performed at different vertical effective stresses by applying a differential water pressure of 1 MPa between the top and bottom side of the specimen. (iv) Then, in order to perform the first gas injection test, the water VPC connected at the bottom side of the specimen was replaced by the gas VPC. Nitrogen (N_2) was used in the experiments. At first, water in the bottom drainage line was flushed out and replaced by gas at an initial pressure of $u_{g,bot}$ = 3 MPa. The sequence comprised then a constant rate gas injection period (0.2 ml/min for an initial gas volume of 500 ml in the reservoir) during which gas pressure was increased from 3 MPa to 10 MPa. Gas pressure was then kept constant until quasi steady state conditions were observed for both gas flow and volumetric response of the tested specimen. Finally, the gas VPC was stopped, ensuring constant gas volume at the inlet, and the resulting gas pressure decay was monitored (so-called shut-in phase). Water back-pressure at the top of the specimen was kept constant during the entire sequence at $u_{w,top}$ = 1 MPa. The maximum gas pressure always remained at least 5 MPa below the total vertical stress in order to avoid preferential flow paths at the interface between the specimen and the oedometer ring. (v) After the gas injection phase, water resaturation was performed under constant vertical total stress, followed by a water permeability test in order to assess the evolution of the intrinsic permeability due to gas transport. This was followed by a second gas injection phase (vi) with a different rate of gas injection period (0.05 ml/min for an initial gas volume of 500 ml in the reservoir) with the aim to observe the response of the specimen under different loading conditions. Finally, the specimen was unloaded and followed by postmortem analyses to determine the final degree of saturation and to characterise the microstructure of the tested material (vii). The test sequences are illustrated in Figure 2-37.

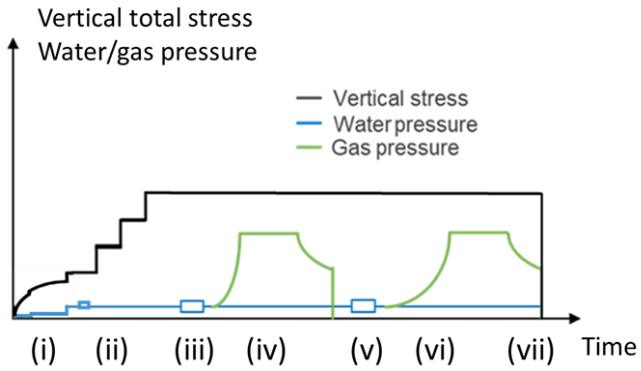

Figure 2-37 – Sequences for the water and gas injection tests.

2.3.5.3 Results

During resaturation, the tested specimen was put in contact with water at low pressure. During water uptake, as the specimen had the tendency to swell, vertical total stress was progressively increased to ensure isovolumetric conditions and minimize damage due to swelling. To enhance saturation, the water pressure was increased up to 1 MPa and a differential water pressure was applied between the bottom and the top of the specimen so that water could flow and flush the trapped gas within the pore space. The stress value when equalization conditions were achieved is called the swelling pressure of the tested material; a value of S_p = 3 MPa.

The one-dimensional compression allowed to assess the relationship between deformation, expressed in terms of void ratio, and the applied stress. Additionally, the water permeability was computed from the one-dimensional consolidation theory for shales (Ferrari et al., 2016). Figure 2-38 shows a decrease of the computed water permeability from the consolidation theory (empty dots) with decreasing void ratio. These results are in line with those obtained from the constant head water permeability tests and computed form Darcy's law (filled dots). The water intrinsic permeability was obtained in the range of $2.7 \cdot 10^{-21}$ m^2.

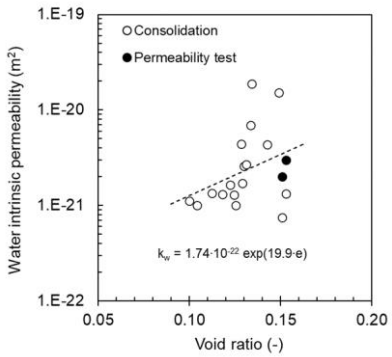

Figure 2-38 – Water intrinsic permeability obtained from constant head permeability tests and from consolidation analyses.

A first gas injection test was performed at a fast gas injection rate with the intention to favour an undrained response of the tested specimen. The controlled boundary conditions, such as vertical stress and fluids pressure/flow rate (gas injection rate and pressure and water back-pressure), as well as the gas pressure decay in constant volume conditions during the shut in are shown in Figure 2-39 (top).

The global axial strain of the specimen computed from the measurement of the vertical deformation, shown in Figure 2-39 (middle), indicates that almost no deformation was observed at the early phase as gas pressure was likely below the gas entry pressure and had not yet invaded the pore space. Once gas reached a pressure of about 5 MPa (t = 17 h), expansion of the specimen was observed, indicating that gas likely entered the pore space, started to displace water and capillary pressure developed. The air entry value was very consistent to the one estimated from the MIP test (see below).

After t = 17 h, expansion continues as gas pressure continued to increase. Once gas pressure was kept constant at 10 MPa (from t = 30.5 h), expansion continued to slightly increase and reached a value of 0.14%, and was followed by a slow reduction and stabilization at about -0.07% (t = 193 h). As gas pressure decreased during the shut-in phase (t > 193 h), the specimen experienced compression. Gas pressure after shut-in was measured at 5.7 MPa.

Those observations on the mechanical response are consistent with the measured outflow from the specimen. Gas breakthrough, which was assessed from the detection of a significant increase of the outflow, was detected only after the maximum gas pressure was reached. This suggests that gas flow was impaired by the low permeability of the specimen, leading to the delayed observation of gas breakthrough (t = 50 h). With time, gas outflow was increasing until quasi-steady state conditions were observed at about t = 193 h. The gas outflow at standard temperature and pressure (STP) conditions was about $2 \cdot 10^{-9}$ m^3/s. During the shut-in phase, gas outflow decreased until almost no flow was observed anymore.

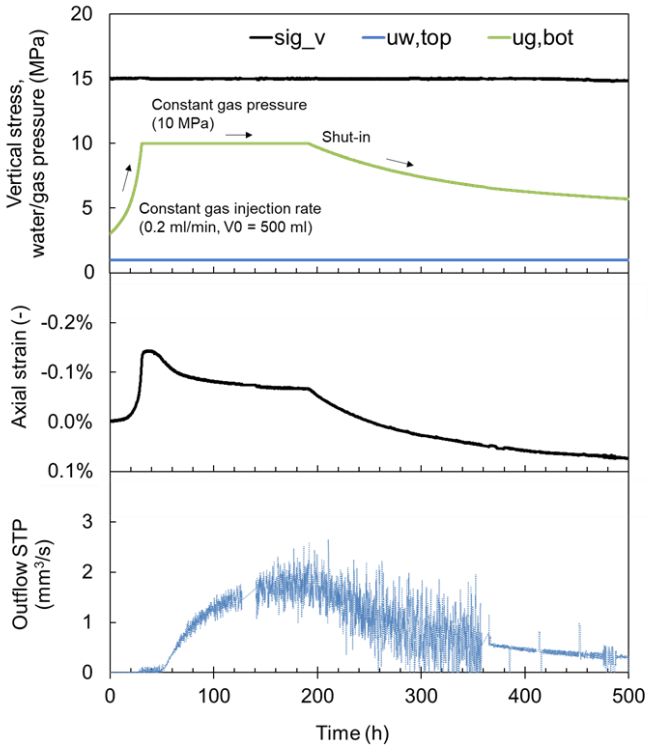

Figure 2-39 – Gas injection test

Resaturation has been performed after gas invasion (sequence v). The water resaturation at constant vertical stress has not shown any significant strain upon water uptake (less than 0.01 %). The water intrinsic permeability computed after resaturation was very similar to the one obtained prior to the gas injection ($2.1 \cdot 10^{-21}$ m^2) and suggests that the permeability of the specimen was not impaired by the gas transport.

To assess the evolution of the microstructure due to the gas invasion processes, MIP tests were performed. Figure 2-40 depicts the pore size density (PSD) function of natural OPA before and after gas invasion. The PSD functions are shown without the correction of the conformance effect in order to compare the results on the whole range of the obtained data. The MIP results showed no marked differences in the pore size distribution on specimens tested before and after gas invasion, indicating no significant modification of the microstructure after gas invasion.

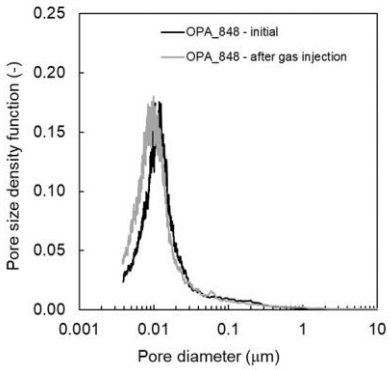

Figure 2-40 – PSD function of natural OPA before and after gas invasion.

2.3.5.4 Conclusion

The experimental work used a high-pressure oedometer cell specifically developed to analyse the hydro mechanical behaviour of geomaterials at high-confining stresses. The assessment of the vertical deformation was done using three LVDTs. When considering laboratory testing of shales, rigorous experimental procedure and test set-up is required due to its low permeability and porosity, high water retention properties, as well as the dependency of the material's behaviour on the saturation state. In this regard, a systematic procedure was adopted to obtain intact specimens for the injection tests.

Observations on gas tests injection suggest that both mechanisms, namely visco-capillary two-phase flow and dilatancy-controlled gas flow, are relevant and necessary to describe the hydro mechanical response of OPA to gas invasion.

Comparison of the water intrinsic permeability and the PSD function before and after gas invasion suggest no significant differences. Therefore, the present results suggest that the barrier function of the host rock is not impaired by the gas invasion processes.

2.3.6 CIMNE/UPC - Hydromechanical response of claystones on gas injections

CIMNE/UPC contributed to the mechanistic understanding of the hydro-mechanical phenomena and processes, associated with:

- Gas-induced failure of clay barriers, including the engineered barrier system, the EDZ and the argillaceous host rock.
- Effectiveness of self-sealing processes along gas-induced pathways in the clay barriers of a geological repository.

All the tests were performed on Boom Clay. Samples were retrieved at the HADES underground research facility URL (Mol, Belgium).

2.3.6.1 Experimental set up

Two different apparatus were used during the project to perform gas tests. A cell was developed for previous research into gas migration in Boom clay (Gonzalez-Blanco et al., 2016; Gonzalez-Blanco, 2017) and has been updated for this project.

The first apparatus is an oedometer cell which, together with the boundary condition controllers and data acquisition system, forms the setup shown in Figure 2-41. The samples (height of 20 mm in a 50 mm diameter ring) are placed between the top and bottom caps made of concentric stainless-steel rings

(number 2 in Figure 2-41), which operate as coarse porous stones allowing the injection and recovery, as well as the proper distribution of the injected fluids (water and gas). At both boundaries of the sample, there are two connections for flushing the fluids contained in the porous stone, when needed. The bottom boundary corresponds to upstream while the top to downstream. A pneumatic axial loading piston (blocking system – number 3 in Figure 2-41), which supports a vertical stress capacity of more than 20 MPa, is used to apply the vertical load.

An automatic pressure/volume controller (PVC) from GDS Instruments (number 4 in Figure 2-41) is connected to the axial piston with a high-strength steel tube to ensure proper transmission of the load and to prevent leakages.

The equipment uses three additional automatic PVCs, two for water (injection and recovery at the downstream point- numbers 5b and 6 in Figure 2-41), and one for gas (injection at the upstream point - number 5a in Figure 2-41). PVCs can be used in combination (for example, gas injection and water pressure at downstream or water pressure at both sides).

Vertical displacements are measured with a calibrated external linear variable differential transformer (LVDT) (number 7 in Figure 2-41).

The data acquisition software was developed in Visual Basic (Microsoft) to monitor the pressures and volumes of controllers and the vertical displacements using an electronic box with a National Instrument Card.

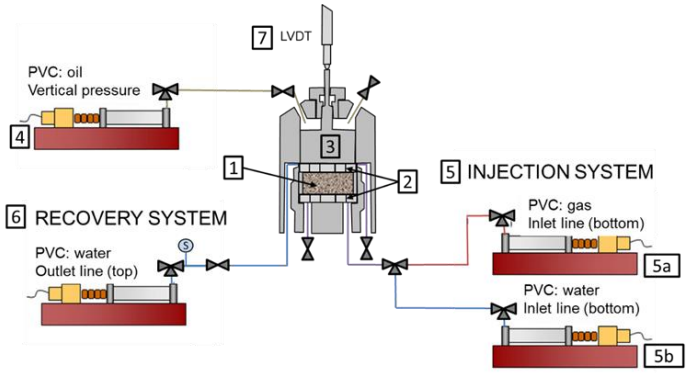

Figure 2-41 – Scheme of oedometer setup: 1) Sample; 2) Coarse porous rings; 3) Hydraulic piston; 4) Oil PVC; 5) Injection system: a) water PVC, b) air PVC; 6) Recovery system: water PVC; 7) LVDT.

A second apparatus was designed and built to evaluate the gas migration processes. It has a double modality and can work as an oedometer cell or an isovolumetric cell, thanks to a blocking system of the pneumatic piston with a load cell, although during this work, oedometer conditions were used. Moreover, the equipment includes a deformable ring that allows the estimation of the radial stresses through the measurement of the radial displacement.

The instrumentation of the set-up has been greatly improved. It includes a pore-pressure transducer, a gas trap system and several sensors to maximise the recorded information during the tests.

The sample (height of 25 mm in a 50 mm diameter ring) (number 1 in Figure 2-42) is placed in the oedometer ring (number 2 in Figure 2-42) between the top and bottom caps made of concentric stainless-steel discs acting as porous stones (number 3 in Figure 2-42), which are placed together with a fluid distributor to properly distribute the injected fluids (water and gas). At the bottom cap, the three connections are standing at 120º-angle which improves the flushing of the fluids contained in the porous stones when it is needed. The bottom cap also hosted a small sintered stainless-steel disc (8 mm in diameter and 2 mm in height) acting as a separator thanks to an O-ring to isolate the chamber where a

pore-pressure transducer is located (bottom of the sample) (number 4 in Figure 2-42). The top cap counts with two connections at 180º-angle (number 5 in Figure 2-42).

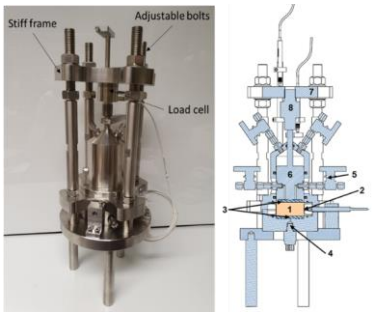

Figure 2-42 – Schematic of the cell.

Boom clay samples have been taken from two cores. The first one was horizontally drilled from Ring 66-67 of the borehole 2012/6 at the HADES (horizontal borehole towards the West) at a depth of 223 m and identified as Core 8 (ID: CGR66-67W_Core 8_Sectiona). The second is identified as Core 12 (ID: CGR74/75D Core 12 11.30-12.08 m) and was vertically drilled from Ring 74-75 of the borehole 2014/1 twelve meters below HADES.

A part of each core was used for determining the geotechnical and initial properties which are summarised in Table 2-14 together with results of previous studies (Gonzalez-Blanco, 2017; Gonzalez-Blanco et al., 2022; Gonzalez-Blanco & Romero, 2022). The air entry value (AEV) indicated in the table, corresponds to the dominant pore mode detected from MIP data and was determined using Laplace's equation.

Table 2-14 – Initial conditions and properties.

Parameter	Previous results (Gonzalez-Blanco, 2017)	New results	
		Core 8	Core 12
Geotechnical properties			
Density of soils, ρ_s (Mg/m^3)	2.67		
Liquid limit w_L (%)	67		
Plasticity index, I_P (%)	38		
Initial conditions			
Density, ρ (Mg/m^3)	2.02-2.06	2.04-2.05	2.01
Dry density, ρ_d (Mg/m^3)	1.63-1.69	1.67-1.69	1.61
Porosity, n	0.37-0.39	0.37	0.398

Void ratio, e	0.58-0.63	0.58-0.59	0.660
Water content, w (%)	22.6-24.0	19.0-20.2	24.18
Degree of saturation	close to 1	0.93-0.96	0.99
Total suction after retrieval, Ψ (MPa)	2.45	3.2-4.4	3.47
Osmotic suction, π (MPa)	0.5		
Increase in matric suction, s (MPa)	0.2	0.95-2.15	1.22
Air-entry value from MIP (MPa)	4.8		
Dominant pore mode from MIP (nm)	65-70		

Table 2-15 contains the initial conditions of samples used in each test. The nomenclature used in the reference consists of: Set of tests (SET1, SET2, SET3 or SET4) - Protocol (A, B, HM, GAS or DAM) – Orientation of bedding planes (N: normal to flow; P: parallel to flow).

Table 2-15 – Sample reference, core and initial conditions for samples used in each test.

Reference	Core	Density	Porosity	Void ratio	Water content
SET1_A_P	CGR66-67W_Core8_Section_a	2.05	0.37	0.59	19.02
SET1_A_N	CGR66-67W_Core8_Section_a	2.05	0.37	0.59	19.27
SET1_B_N	CGR66-67W_Core8_Section_a	2.05	0.37	0.58	20.21
SET2_HM_N	CGR74/75D_Core 12	2.05	0.37	0.58	24.18
SET2_HM_P	CGR74/75D_Core 12	2.07	0.36	0.56	23.70
SET3_GAS_N	CGR74/75D_Core 12	2.06	0.37	0.58	21.64
SET3_GAS_P	CGR74/75D_Core 12	2.06	0.36	0.57	22.40
SET4_DAM_N	CGR74/75D_Core 12	2.07	0.36	0.57	19.66
SET4_DAM_P	CGR74/75D_Core 12	2.07	0.36	0.57	19.66

Synthetic Boom Clay water was prepared according to De Craen et al. (2004). Air (21% O2 and 79% N2) and Helium (purity >99.999%) have been used as testing gases.

2.3.6.2 Testing protocols

CIMNE's experimental programme on Boom Clay addressed the basic phenomena and processes related to gas transport when gas pressure is below confining pressure and contributed to gaining knowledge of the self-sealing mechanisms at the process level. The proposed experiments combined water/gas injection experiments under oedometer conditions. The protocols were developed to assess the following issues:

- Derivation of constitutive relationships of the water retention behaviour and stress-strain relationships in response to gas invasion processes.
- Validation of existing concepts of constitutive stress (e.g. net stress, Bishop's formulation) for their applicability to gas invasion processes.
- The investigation of the re-saturation process ("imbibition of the wetting fluid") after the gas invasion.
- Studying the possible loss of hydraulic integrity by comparing water permeability before and after gas injection.
- Evaluating the effect of a second injection after re-saturation.
- Determining the self-sealing capacity on previously damaged samples (by loading/unloading) and possible fissure re-activation upon gas injection.

Table 2-16 gathers the main stages of each protocol.

Table 2-16 – Stages of the different protocols.

Stage	SET 1-A	SET1-B	SET 2	SET 3	SET 4
1	Pre-conditioning	Pre-conditioning	Pre-conditioning	Pre-conditioning	Pre-conditioning
2	Drained loading	Drained loading	Water permeability	Drained loading	Drained loading
3	Water permeability	Water permeability	Drained loading	Water permeability	Water permeability
4	Gas injection	Gas injection	Drained unloading	Gas injection	Drained unloading
5	Re-saturation	Re-saturation	Drained reloading	Re-saturation	Drained reloading
6	Water permeability	Water permeability	Water permeability	Water permeability	Water permeability
7	Undrained unloading	Gas injection	Undrained unloading	Gas injection	Gas injection
8	Postmortem analyses	Undrained unloading		Undrained unloading	Re-saturation
9		Postmortem analyses		Postmortem analyses	Water permeability
10					Gas injection
11					Undrained unloading

The main stages for Protocol were:

- Pre-conditioning

Initially, samples were loaded close to representative in-situ stress-state conditions (~2,5 MPa). The pre-conditioning paths are mandatory to reach the geostatic conditions of the material in the in-situ state, which were the starting point of any test, ensuring the most similar stress state. These paths consisted mainly of loading the samples up to a pre-defined stress level at constant water content reducing the initial matric suction and afterwards, flooding the sample with synthetic water. The samples could undergo expansion and degradation as a clear consequence of suction reduction effects due to water contact at low stress levels. To minimise these effects, the samples were always loaded to a target total stress of 3 MPa and only then put in contact with water under atmospheric pressure to avoid any damage. After reaching steady-state conditions, water pressure at the downstream and upstream boundaries was increased from 0 (atmospheric pressure) to 0.5 MPa and hence, once the pore pressure was equalized, the effective stresses were equivalent to the in-situ ones.

- Drained loading

The samples were loaded at drained conditions (the absence of pore water pressure increase was checked by stopping the load and recording the displacements, which were negligible) at a rate of 0.5 kPa/min up to a maximum total vertical stress of 6/8 MPa. This vertical stress was kept constant.

- Water permeability determination

After ensuring full saturation, water permeability was measured by applying a hydraulic gradient. Water pressure at the bottom side was increased from 0.5 to 0.6 MPa to induce the flow of water through the sample. Downstream pressure remained constant (0.5 MPa, this top cap pressure was maintained constant along the different stages of the test). Axial deformation was monitored along this hydraulic process. Water permeability was measured under steady-state conditions using the water volume information at the inflow and the outflow. After that, the backpressure was reduced to 0.5 MPa again until stabilization.

- Gas injection

Firstly, water pressure in the upstream vessel was reduced to atmospheric conditions to allow for its fast replacement by gas. Gas pressure at the upstream point was rapidly increased from atmospheric conditions to a value of 0.5 MPa.

Gas injection from an initial pressure of 0.5 MPa to a maximum gas pressure below the lateral stress was applied at different constant flow rates (2 mL/min or 100 mL/min). Once reaching the maximum gas pressure, the injection system was stopped (shut-off) and a recovery phase at constant gas volume started until gas dissipation. In the case of using the oedometer with lateral stress measurement, the lateral stress variations were estimated from the thin wall of the ring movement. Information on gas volume at the inflow was recorded. At the outflow, the gas trap accounted for the volume of gas and displaced water (if any).

- Re-saturation

After gas injection, a re-saturation stage was carried out. The top and bottom caps were firstly filled with water at atmospheric pressure. A small hydraulic gradient was applied to displace the gas that might be stored in the sample. This process lasts until stabilization.

- Water permeability determination

After ensuring full saturation, the hydraulic gradient was increased to impose a water flux. Axial deformation was monitored along this hydraulic process. Water permeability was measured under steady-state conditions using the water volume information at the inflow and the outflow.

- Undrained unloading

Gas pressure in the upstream vessel was reduced to atmospheric conditions as well as the fluid pressure in the downstream vessel. Simultaneously, vertical stress was decreased under undrained conditions to preserve the samples and track possible microstructural changes due to gas passage.

- Postmortem analyses

A microstructural study of the samples after the tests was carried out, with two different techniques: Mercury Intrusion Porosimetry (MIP) and Micro-Focus X-ray Computed Tomography (µ-CT). Freeze-drying of the sub-samples is mandatory for the two first techniques, while µ-CT is performed on sub-samples with the final water content.

2.3.6.3 Results

In this paragraph and for the purpose of this report, results presented are focus on water permeability before and after hydromechanical-gas solicitations. For details results, see dedicated report from EURAD-GAS.

Figure 2-43 shows the water permeability estimated at the in-situ stress level and after the drained loading to 6 MPa as a function of the average void ratio for each sample. The results are in good

concordance with the previous data (unfilled marks in the figure) (Gonzalez-Blanco & Romero 2022), and highlight a clear dependence of the water permeability on the porosity especially for orientation perpendicular to the bedding planes. Furthermore, as expected, higher water permeability was observed with flow parallel to bedding planes, indicating a marked anisotropic feature.

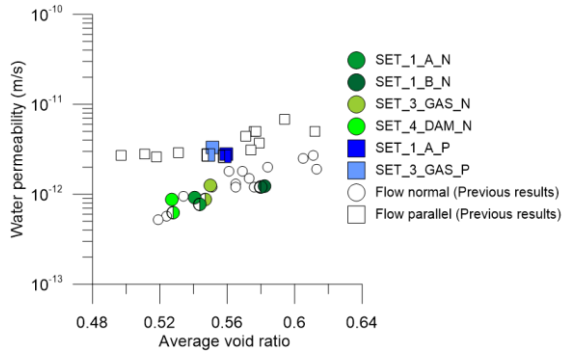

Figure 2-43 – Hydraulic conductivity results as a function of the void ratio.

For SET 2 and SET 4 of experiments, water permeability was measured at various stress levels before and after the loading/unloading cycle. It can be observed (Figure 2-44) that water permeability at the in-situ stress level (~3 MPa for all samples) and after the first loading to 6/8 MPa was equivalent for both bedding orientations, keeping the anisotropy feature. In contrast, the loading/unloading cycle caused a significant decrease in water permeability.

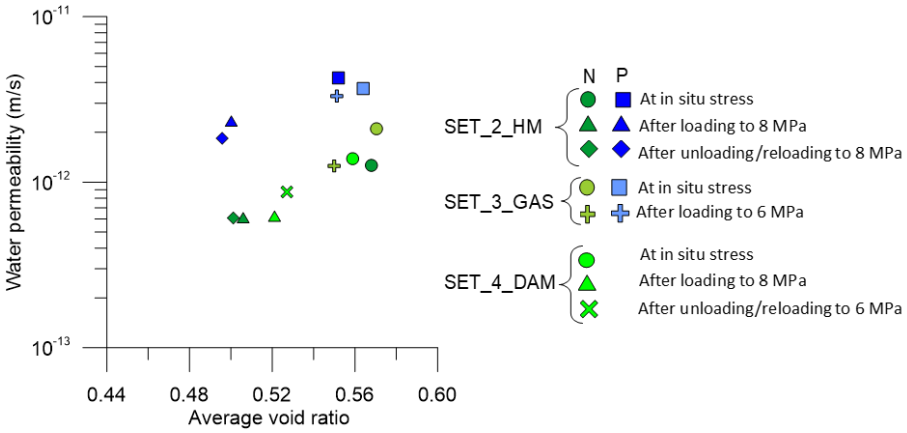

Figure 2-44 – Water permeability after different hydro-mechanical paths for samples at both orientations.

After the gas injection and dissipation stage, the samples from SET 1, 3 and 4 were put in contact with water under atmospheric pressure until they reached steady-state conditions. During this stage, the deformation was very small (less than 0.05%), confirming that no significant desaturation occurred during the gas transport (Figure 2-45).

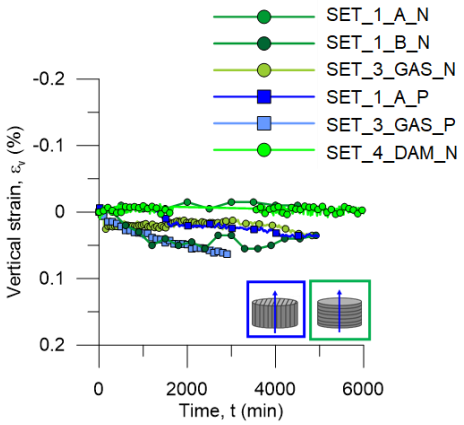

Figure 2-45 – Strain evolution during the re-saturation stage.

After stabilisation, water permeability was measured again by applying a hydraulic gradient at constant vertical stress (downstream and upstream water pressures were increased up to 0.6 MPa and 0.5 MPa, respectively). Figure 2-46 shows the results of this stage in comparison with the results obtained before the gas injection. For each sample, the water permeability values did not present significant changes, which might entail an excellent self-sealing of the fissures that formed during gas injection due to the re-saturation process. As the re-saturation was done under constant vertical stress, the driving mechanism of self-sealing is the swelling of clay minerals, although some creep could also contribute to the closure of the fissures. From these results, it can be concluded that Boom Clay's self-sealing capacity is significant in recovering the hydraulic barrier function.

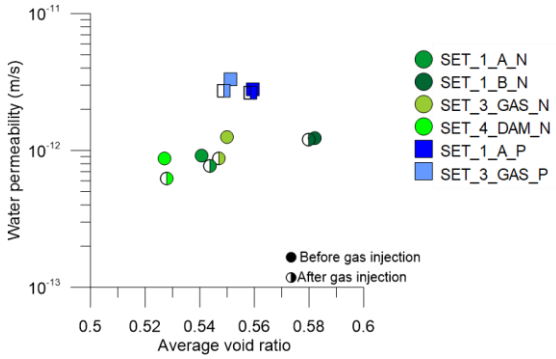

Figure 2-46 – Water permeability before and after gas injection.

The microstructure of the samples was analysed through Mercury Intrusion Porosimetry (MIP) and micro-computed tomography (μ-CT), and the findings were compared with those presented in Gonzalez-Blanco and Romero (2022) for the initial state and after the gas injection tests. Representative sub-samples were meticulously trimmed from oedometer specimens after tests and under unstressed conditions. Two distinct shapes were considered for the analyses: a cubical shape of 1000 mm³ for MIP and a cylindrical shape measuring 10 mm in height and 10 mm in diameter for μ-CT tests to avoid corner artefacts. In both cases, the samples underwent a freeze-drying process, essential for MIP, to facilitate results' comparison.

The Pore Size Density curves (PSDs) obtained with MIP for the intact state exhibited a monomodal distribution with a dominant size of 70 nm and a low volume at the macro-scale. In contrast, samples after gas injection tests in previous research campaigns (Gonzalez-Blanco et al., 2017; Gonzalez-Blanco & Romero, 2022) consistently revealed a new family of large pores. These larger pore sizes, exceeding 2 µm, were linked to the expansion experienced by Boom Clay samples during gas injection and early shut-off stages, as well as the dilation of gas pathways. These PSDs are now compared with the ones obtained after re-saturation (SET_1_A) and after the second gas injection stage (SET_1_B and SET_3) (Gonzalez-Blanco et al., 2023). In Figure 2-47, the PSD curves are presented in a log-log plane to highlight the larger pore sizes. After re-saturation, lower volumes at the macro-scale were observed compared to samples after gas injection for both bedding orientations. However, these volumes were still slightly higher than those corresponding to the intact sample, suggesting that there was no complete healing of the material during re-saturation, and some pores or fissures did not completely close. On the other hand, the PSD of the samples after the second gas injection revealed the highest volume at the macro-scale.

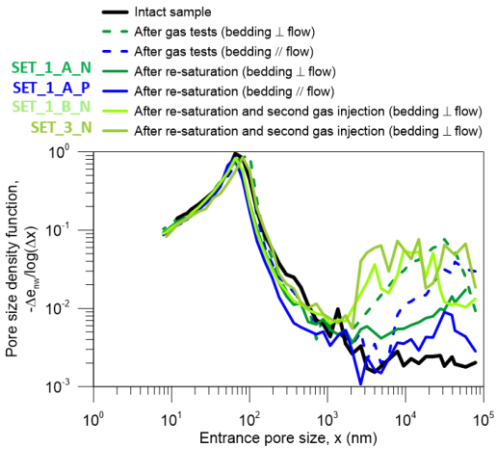

Figure 2-47 – Pore size density curves from MIP on the intact sample, samples after gas injection tests, samples after re-saturation and samples after second gas injection.

To provide a comprehensive overview that facilitates the understanding of microstructural evolution due to different processes, Figure 2-48 compares µ-CT images for samples with bedding planes parallel and normal to the flow at the initial state, after gas injection, and after re-saturation. It also includes an image of the sample with bedding planes normal to the flow after a second injection.

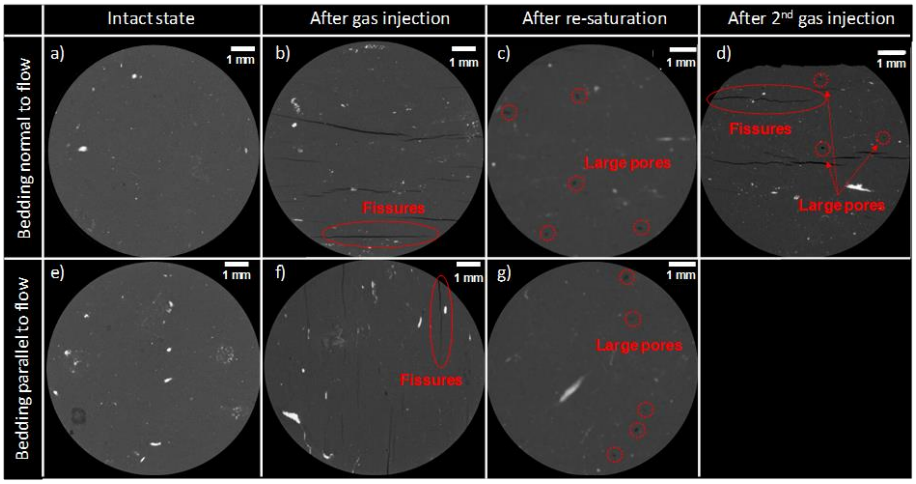

Figure 2-48 – Cross-section µ-CT images of Boom Clay samples. Top: sample with bedding planes normal to flow a) at the intact state (Gonzalez-Blanco & Romero 2022); b) after gas injection (Gonzalez-Blanco & Romero 2022); c) after re-saturation; d) after second gas injection (Gonzalez-Blanco et al 2023). Bottom: sample with bedding planes parallel to flow: e) at the intact state (Gonzalez-Blanco & Romero 2022); f) after gas injection (Gonzalez-Blanco & Romero 2022); g) after re-saturation (Gonzalez-Blanco et al 2023).

For the intact state, only a very small volume of pores is identifiable, and bedding planes are not visible at the current resolution. After gas injection, samples in both orientations exhibit fissures in the direction of the bedding planes. The analysis of the fissure network (Gonzalez-Blanco & Romero, 2022) revealed that in the sample with bedding planes parallel to flow, the fissures are closer and have a lower mean aperture than in the opposite orientation. This is because radial deformation was restricted by the oedometer conditions. However, the fissure density was remarkably similar for both orientations, indicating no significant orientation effects during gas transport, consistent with the results on effective gas permeability that did not show anisotropy.

After re-saturation, the fissures self-sealed in both orientations, but as mentioned earlier, some large pores remained after this process. Again, the volume detected is quantitatively similar for both orientations.

In the case of the sample subjected to a second injection, the mean aperture of the fissures is slightly higher than after the first gas injection, consistent with the higher gas permeability. This is a consequence of some memory of the fissure network developed during the initial gas injection, which involved mechanical damage to the material (Gonzalez-Blanco et al., 2023). Additionally, the pores with entrapped gas could have formed due to the non-uniform closure of the pathways during re-saturation. It is essential to note that the microstructural analyses were performed after an undrained loading, and as a result, these air-filled macro-pores could be enlarged during this phase, as the volume of entrapped gas under stress conditions might not be insignificant.

2.3.6.4 Conclusions

An experimental campaign was launched using a multi-scale and hydro-mechanical coupled methodology. Gas injection and dissipation tests under oedometer conditions in saturated deep Boom Clay were carried out. Relatively fast controlled-volume rate gas injection tests (gas pulse tests) were performed in order to study gas flow mechanisms associated with the opening of stress-dependent pathways. The tests were conducted on samples with oriented bedding planes (parallel and orthogonal to the flow), varying gas injection rates and stress states, with the aim of investigating their impact on

the coupled hydro-mechanical mechanisms that govern gas transfer. The experimental setups permitted volume changes, and the deformation response was studied throughout the stages of gas pressure increase and dissipation.

The quantity of water displaced by gas during the gas injection/dissipation stages was measured using an advanced gas trap system. The results reflected that the majority of the fluid collected upstream was gas together with a residual amount of water that only meant a small desaturation of the clay matrix. This fact reinforced the idea of gas transport through preferential pathways.

The microstructural study after gas tests by using complementary techniques (MIP and µ-CT) confirmed the opening of fissures with varying apertures and separations and confirmed the opening of fissures with large apertures (> 40 µm), primarily developing along weaker bedding planes.

The mechanism for gas transport with bedding planes orthogonal to flow appeared to be driven by low-aperture fissures with narrower separations connecting non-perfectly parallel bedding planes. Therefore, it was considered that these inter-bedding and low-aperture pathways were also very efficient in gas transport, as indicated by the effective permeability to gas showing no clear anisotropy.

The ability to self-seal of Boom Clay was assessed since it is a property that impacts the hydraulic barrier function of radioactive waste disposal systems. The effectiveness of the self-sealing was evaluated by comparing water permeability before and after the gas invasion. The initial water permeability was determined under oedometer conditions for samples with two bedding orientations: parallel and normal to the flow, displaying a distinct anisotropic behaviour. Notably, samples with bedding planes favourably oriented to the flow (parallel) exhibited higher initial water permeability. Following this, the samples underwent a gas injection and dissipation stage at constant vertical stress. As explained above, this gas invasion led to the development of pressure-induced fissures. During re-saturation, very small deformations were recorded pointing out to the closure of the localised gas paths. The re-saturation of the samples at constant vertical stress resulted in the restoration of the initial permeability for both orientations, replicating the original anisotropy. This was considered evidence of the Boom Clay's effective self-sealing capacity. However, complete self-healing was not conspicuous, as microstructural analyses revealed higher volumes at the macro-scale than in the initial state. This could be attributed to potential gas entrapment or occlusion in large pores, which were not entirely closed during re-saturation. Nevertheless, these pores did not exhibit connectivity, aligning with the restoration of the initial permeability.

In a further step, the effect of a subsequent gas injection stage was addressed in order to study possible fissure reactivation during gas transport after self-sealing. The effective gas permeability measured in this stage was the highest, aligning with the largest volume of pores at the macro-scale as detected by MIP. Analyses of µ-CT images revealed the opening of large-aperture fissures in the direction of the bedding planes, and with improved resolution, low-aperture fissures bridging the bedding planes were also identified. Furthermore, some large pores were discerned in the images, likely associated with gas entrapment during the initial injection and subsequently enlarged during undrained unloading. These observations suggest that the second episode of gas invasion could reopen the fissures, facilitating the flow of gas with greater ease.

3. Modelling

Only one team, ULiège, developed a specific model to take into account the self-sealing in clay host rock. This model considers the consequences of hydration or drying on the fracture materials and introduces hydromechanical coupling behaviour of the damaged materials. In the model, gas transfer and temperature effects related to self-sealing have not been considered.

3.1 ULG

Based on experimental evidence, ULG defined a constitutive model able to describe and predict the self-sealing in clayey rocks. In this context, several tests have been performed under different conditions showing self-sealing efficiency in clay host rocks (Bock et al., 2010; Di Donna et al, 2022; Wang et al, 2022; Zhang et Talandier, 2023). At the laboratory scale, it was observed that the main mechanisms responsible for the self-sealing are the swelling of clay minerals, the consolidation and creep (Bernier et al., 2007a). The process is therefore strictly related to the main properties of the potential host rock.

Despite the large number of experiments, limited attempts were made to model this phenomenon numerically. A numerical approach in this field is necessary to describe and understand the hydro-mechanical behaviour of the fracture, and to predict the self-sealing process in the long term.

ULG defined a 2D constitutive model able to describe the sealing capacity of the Cox claystone, accounting the clay swelling around the fracture as well as the role of its initial size. The main phenomenological aspects involved during the self-sealing are call back. Then, the finite element code LAGAMINE is used to validate the model against laboratory tests under pseudo-oedometric conditions. In the proposed model, the anisotropy of the material, but also the chemical properties of the saturation water are not considered. They both deserve to be implemented in future extensions of the model. Moreover, in a first version it is defined in 2D, describing a vertical section of a sample. This simplification is justified because the selected laboratory tests are carried out on cylindrical samples with a planar fracture. Then, a validation with a 3D model is also executed. This 3D version should be properly improved for further studies at the repository scale.

3.1.1 Definition of the interface element

The intact clay is modelled in the framework of the continuum mechanics and is assumed as a linear elastic material, while the fractured zone is modelled using a zero-thickness interface element. This interface element is widely used in modelling joints and rock discontinuities in the framework of finite element methods since it is suitable for large deformations without re-meshing. It has also been used to model the interface between two different media as well as in rock fracture mechanics. The contact zone is discretized through field nodes and is only activated in the case of contact. An accurate description of this type of contact element is provided by Cerfontaine et al. for a 3D problem, while a 2D schematization is given in Figure 3-1. The zero-thickness element is discretized by the three-node method, i.e., the interface element includes the inner of the discontinuity (index F) and the two adjacent sides (indexed C1 and C2) allowing the modelling of the fluid flow propagation along and through the discontinuity (fl and fti in Figure 3-1b). Each node of the two sides (i.e., nodes 1–6) carries 3 degrees of freedom (the displacements ux and uy in the horizontal and vertical direction, respectively, and the pore water pressure pw). Each inner node (i.e., nodes 10 –30) is fixed in terms of displacement and thus carries only the pore water pressure degree of freedom. This discretization allows a homogenous field of pressure across the interface while there is a transversal drop of pressure between the two sides of the fracture. The fracture opening d in Fig. 3b is measured as the distance between the nodes of the side C1 and those of C2 and is computed through a segment-to-segment discretization as described in Cerfontaine et al.

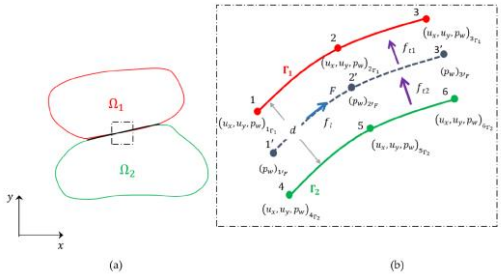

Figure 3-1 (a) Contact between two continuum deformable solids X1 and X2; (b) Definition of the parabolic three-node discretization of an interface element where C1 and C2 are the side of the interface (nodes 1–6), F is the inner of the interface (nodes 10 –30 obtained as the projection of nodes 1–3 of the side C1)

3.1.2 The hydro-mechanical formulation for the fracture

3.1.2.1 Mechanical behaviour

The fracture mechanical behaviour is described by the Mohr Coulomb frictional law:

$$f \equiv \tau - (c + \mu p_N) = 0$$

where τ and p_N are, respectively, the tangential and normal pressure, c is the cohesion, and $\mu = \tan(\phi)$ is the friction coefficient. The function f can be considered as a yield surface defining three different zones, as illustrated in Figure 3-2a

- f < 0: sticky contact (pseudo elastic behaviour)
- f = 0: slip contact (yield surface)
- f > 0: impossible state

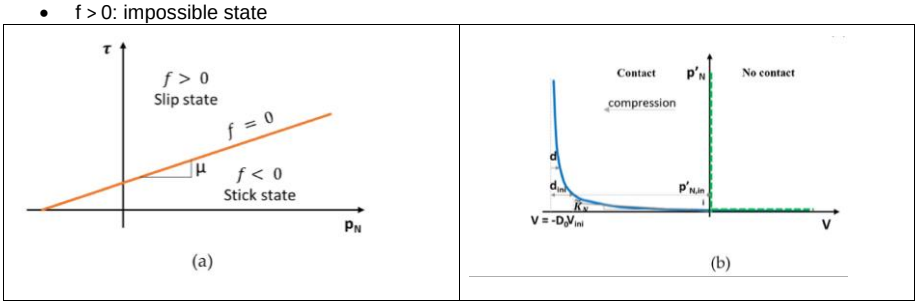

Figure 3-2 Mechanical behaviour at the interface: (a) Coulomb contact law; (b) normal behaviour in terms of fault closure V—effective normal contact pressure p'_N In (b) the green dot line represents the ideal case, while the continuous blue line stays for the real case of a rough interface. The values V_{ini}, d_{ini} and p'_{Nini} indicate, respectively, the closure, hydraulic aperture and the contact pressure at the beginning of the test.

In the normal direction, the fracture mechanical behaviour is defined in terms of variation of the normal contact pressure with the fracture closure V (or the hydraulic aperture d). When two perfectly smooth continuum elements are not in contact, the closure V takes positive values. If the two parts come into contact, their contact pressure increases while the distance V between them cancels (green dot curve in Figure 3-2b). The nonlinear mechanical behaviour of the fracture as represented in Figure 3-2 (in blue) is represented in terms of effective normal pressure p'_N.

If two bodies initially not in contact get closer and closer, their asperities begin to touch and deform, with large displacement for low stress. This behaviour is described through the initial slope $\widetilde{K_N}$ defining a linear relationship between the normal contact pressure and the closure. Then, the applied stress progressively induces smaller and smaller deformations since the fracture is closing more and more, and the number of asperities in contact increases.

- If there is no contact, the hydraulic closure V is zero, while the hydraulic opening d is equal to the mechanical asymptotic closure D_0 ($p'_N = 0 \rightarrow V = 0$; $d = D_0$);
- If the contact pressure reaches large values, then the hydraulic closure V reaches mechanical asymptotic closure D_0, while the hydraulic opening d becomes null ($p'_N = \infty \rightarrow V = D_0$; $d = 0$).

3.1.2.2 Hydraulic behaviour

The three-node discretization introduced above allows the description of the fluid flow (e.g., water in this particular case study) considering as a variable the pore water pressure inside the interface and on the two sides in contact. In this way, it is possible to calculate the longitudinal flow along the discontinuity and the transverse flow inside the interface (Figure 3-1). The liquid water flow along the discontinuity is described by Darcy's equation.

The unsaturated behaviour of a material is described by its water retention curve. In this case, since the two damaged sides are very narrow, they are assumed to follow the same flow equations and retention curve as the intact material. It is assumed that the water retention curve inside the discontinuity is represented by the Van Genuchten relation with air entry pressure depending on the fracture aperture.

Water can also flow through the two adjacent surfaces as a function of the transversal permeability of the fractured material (i.e., the transmissivity) and the difference in pressure between the discontinuity and its two counterparts. According to Figure 3-1, the two transversal flow are:

$$f_{w_{t1}} = \rho_w T_{w_1} t_{rw_1} (p_{w_F} - p_{w_{\Gamma 1}})$$
$$f_{w_{t2}} = \rho_w T_{w_2} T_{rw_2} (p_{w_{\Gamma 2}} - p_{w_F})$$

The transmissivity coefficient is defined as the product between the intrinsic and the relative value, i.e., T_{wi} and t_{rwi}, respectively. They depend on the fluid and rock properties and should be adequately calibrated. The intrinsic transmissivity coefficient T_{wi} is a constant of the material and must take into account the transfer between the fluid in the fracture and the two counterparts. When liquid water is considered, the transfer is faster than with vapor water because, in the latter case, some mass exchanges must occur at the wall of the counterparts. The relative value t_{rwi} is a dimensionless parameter function of the degree of saturation, accounting for the water transmissivity in a two-phase flow (e.g., the water permeability in an unsaturated medium).

3.1.2.3 The hydro-mechanical coupling

The hydraulic and mechanical formulations are coupled through the Terzaghi's effective stress principle under unsaturated conditions. On the other side, the flow properties of the fracture are strongly dependent on its aperture by the mean of the cubic law, defining the fluid flow proportional to the cubic of the fracture opening d.

$$K_{w_F} = \frac{d^2}{12}$$

The calculation of the hydraulic opening d during the re-saturation process requires further investigation. The hydration of the fracture induces some micro-cracks around it (Figure 3-3a), defining a damaged zone able to swell quickly, favouring the hydraulic closure of the fracture. The thickness of this zone depends, for the same material, on the initial thickness of the fracture. Hence, since the area around the discontinuity contributes to self-sealing, it must be considered when describing the interface constitutive

behaviour. The modelling of these damaged sides requires further numerical effort. Nevertheless, since they are narrow enough compared to the sample sizes (about the same order of magnitude as the initial fracture opening), they do not need to be explicitly meshed. This evidence allows to implement them directly in the interface element with considerable numerical simplification, as illustrated in Figure 3-3b.

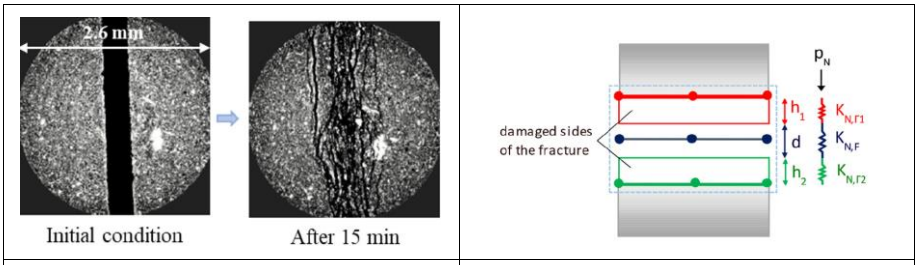

(a) (b)

Figure 3-3 (a) X-ray images of a fractured Callovo–Oxfordian cylindrical sample (horizontal sections) at different time steps of a hydration test (Di Donna et al, 2022) (b) Sketch of the interface element accounting for the damaged area around the main fracture

This aspect is simulated numerically by including two deformable zones into the interface element: the stiffness of the two sides, Γ_1 and Γ_2, are $K_N(\Gamma_1)$ and $K_N(\Gamma_2)$ respectively, while inside the interface, the stiffness is computed with:

$$K_{N_{\Gamma 1}} = \frac{1}{h_{1,\mathrm{ini}}}\left(\frac{1+e_{\mathrm{ini}}}{\kappa_{el_{\Gamma 1}}} p'_{N\mathrm{ini}_{\Gamma 1}}\right)$$
$$K_{N_{\Gamma 2}} = \frac{1}{h_{2,\mathrm{ini}}}\left(\frac{1+e_{\mathrm{ini}}}{\kappa_{el_{\Gamma 2}}} p'_{N\mathrm{ini}_{\Gamma 2}}\right)$$

where e_{ini} is the initial void ratio, $p'_{N,ini\Gamma 1}$ and $p'_{N,ini\Gamma 2}$ are the reference effective mean pressures (assumed equal to the respective values at the beginning of the test) and $K_{N\Gamma 1}$ and $K_{N\Gamma 2}$ are the elastic coefficients, which should be calibrated numerically.

Since the thickness of these damaged boundaries is relatively small, isotropic behaviour is assumed whereby the stiffness moduli are derived from the modified Cam Clay model (Roscoe and Burland, 1968) and normalized by their initial thickness, i.e. $h_{1,ini}$ and $h_{2,ini}$ respectively.

3.1.3 Numerical model

The hydro-mechanical modelling of fractured Cox samples is performed in 2D plane strain conditions by using the finite element code LAGAMINE (Charlier, 1987), (Collin, 2003). The hydraulic and mechanical behaviour as well as contact element were implemented in the code. The validation of the interface model requires the calibration of its parameters and the comparison with some laboratory tests. The following hydraulic paths are selected for this purpose:

- Wetting test (Wang et al., 2022): water is injected into the fracture starting from the initial unsaturated condition.
- water vapor - wetting – drying test (Di Donna et al., 2022): the sample is firstly saturated by water vapor and then by liquid water, and finally, it is dried by injecting dry air.
- Drying–wetting test (Di Donna et al., 2022): the sample is firstly dried and then re-saturated by injecting liquid water.

All the experimental tests used for calibration and validation were conducted on cylindrical samples artificially fractured, as illustrated in Figure 3-4a. The sample was contained in a rigid shell to prevent lateral deformation. To assess only the effect of re-saturation on the hydraulic recovery, no confining pressure was imposed. The sample fracture is oriented parallel to the bedding plane. Since the modelling was carried out in 2 dimensions, only a vertical slice of the sample was considered, as

illustrated in Figure 3-4a, meaning that the anisotropy of the material is not taken into account. The geometry, mesh, and boundary conditions are schematized in Figure 3-4b.

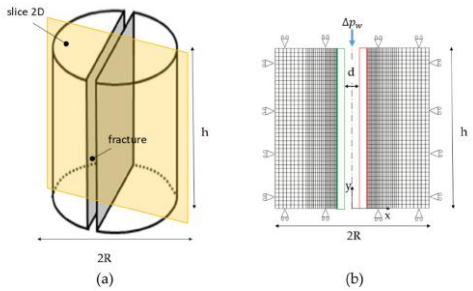

Figure 3-4 Construction of the model: a Sketch of a cylindrical sample prepared and fractured artificially, the vertical slice (in light yellow) is used for the 2D model construction; b 2D model with the definition of mesh, boundary conditions, and water injection Dpw (the dimensions of the damaged elements and the aperture of the fracture are out of scale for schematization purposes)

3.1.4 Results

After a first stage of calibration to obtain the hydro-mechanical parameters, several tests have been performed. Wetting tests results are plotted in Figure 3-5 regarding the temporal evolution of mean hydraulic opening compared with the experimental results. As illustrated in Figure 3-5, procedure used to fit parameters and the proposed model can fit the hydration tests successfully and reproduce self-sealing in the Callovo-Oxfordian claystone for samples from the clay rich unit. It can be observed that the larger the initial fracture size, the smaller the sealing effect obtained.

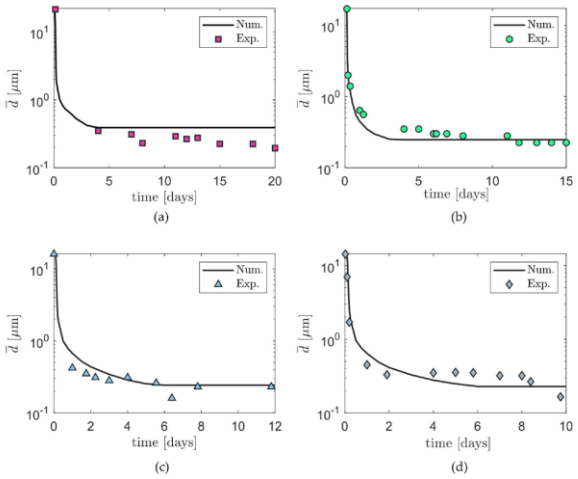

Figure 3-5 Temporal evolution of the average fracture opening during the wetting test, comparison between numerical and experimental results obtained by (Wang et al., 2022a): (a) Test UA1-C; (b) Test UA2-C; (c) Test UA3-C1; (d) Test UA3-C2

Several experimental tests coming carried out by Di Donna and co-authors, as detailed in (Di Donna et al., 2019) and (Di Donna et al., 2022) have been modelled. These tests have been conducted with

different scenarios with successive drying and wetting sequences. For example, in one test, the sequence consists in injecting first some dry air and then resaturating with liquid water. The initial fracture size is 285 µm for the present case study. If the sample is firstly de-saturated, the drying does not induce any visible damage around the discontinuity, at least for the duration of the considered experimental test. Then, the hydration generates a well-defined damaged area around the fracture.

The experimental and numerical variations of the fracture opening with time are displayed in Figure 3-6. Numerically, the aperture varies almost linearly with time. The hydration phase generates secondary cracks around the primary discontinuity that favor the hydraulic closure of the fracture: the opening d decreases very quickly at first and then more and more slowly. The same trend is observed numerically. The final equivalent water permeability reached (Figure 3-6) is a few orders of magnitude higher than the permeability of the intact material. Although the temporal evolution of the opening during drying does not follow the same behaviour observed experimentally, there is a good match at the end of this phase. Afterward, almost at the end of the re-saturation process, a good match between numerical and experimental displacement is observed in the whole section of the sample.

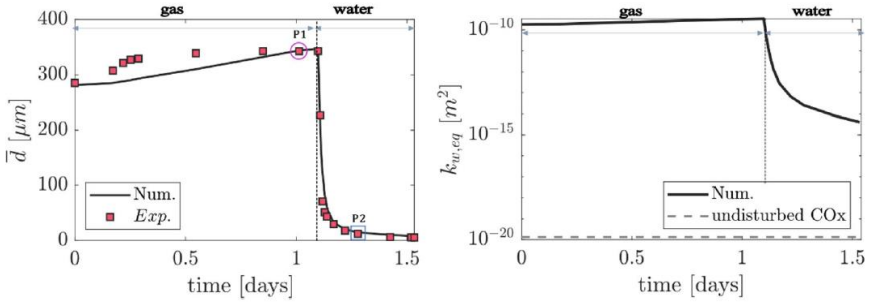

Figure 3-6 Temporal evolution of the average fault opening during test 818, the experimental results refer to (Di Donna et al., 2022) and equivalent water permeability

The 2D model was extended in 3D. The model is validated performing firstly the same wetting tests then, a further analysis was done in order to validate the 3D model against tests conducted by (Zhang and Talandier, 2023) on Cox, where the hydraulic closure of the fracture is correlated to an imposed confining pressure.

The same hydromechanical laws defined in 2D apply for the 3D case, as well as the same sets of parameters. For the sake of simplicity, in a first moment the 3D sample is schematized as a cubic domain characterized by an equivalent cross section equal to the sample area. This simplification is necessary in order to avoid, at least initially, the introduction of complex boundary conditions that would require considerable numerical effort. In a second step, the model could be further enriched to represent in-situ conditions.

3.1.5 Conclusion

The model proposed is able to describe the self-sealing in the Callovo Oxfordian Claystone though a hydro-mechanical constitutive model based on some physical observation of the process. The saturation phase generates micro-cracks around the fracture, defining a low-density and fairly compressible zone, which is even more evident when the initial size of the fracture is large. Thanks to the clay transmissivity, the injected water can permeate the clay, first involving the damaged zone and then the rest of the sample. This process is clearly demonstrated by both numerical and experimental results. However, the bigger the initial crack, the lower the recovery. Figure 3-7 shows the final fracture aperture d_f against the initial one d_{ini}. It is fairly straightforward to see that the model is capable of reproducing the self-sealing satisfactorily for a low initial aperture d_{ini}. However,some tests performed on samples with a high initial aperture value, are more complex, as they include a vapor and gas injection phase in addition to the

saturation phase with water (samples 3132 and 8182 on Figure 3-7) . These phases were reproduced numerically by controlling the water pressure in the fracture and without taking into account the real nature and the chemical composition of the fluid injected, thus could explain the slight offset from the experimental results. The fracture closure dramatically reduces the water permeability, reaching values close to the intact material.

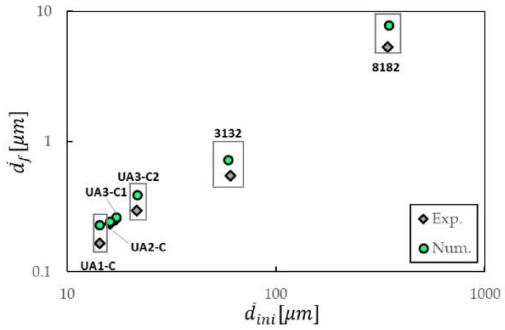

Figure 3-7 Variation of the averaged final fracture d_f as a function of the initial value d_{ini}

The sensitivity analysis shows that the self-sealing occurs even without considering micro-cracks around the fracture, however, the process is slower and results do not match experiments properly. Moreover, the choice of integrating them into the interface elements avoids their re-meshing, with a considerable simplification of the problem.

4. Conclusion

This objective of this program developed during the EURAD project was to evaluate the consequences of temperature and gas on self-sealing capacity of three clay host rocks and a bentonite material.

Several experiments were conducted by seven partners covering different kinds of situation. These laboratory experiments performed in the GAS and HITEC work packages confirm the good self-sealing capability of three clay host rocks, the Boom Clay, the Callovo-Oxfordian claystone and the Opalinus Clay. After exposure to water, the permeability of fractured clay rocks decreases rapidly (in a matter of hours or days) and becomes close to that of the intact rock even if they have been submitted to gas flow or to temperature.

For clay host rock, the self-sealing capacity could depend on the mineral composition of the material. It has been shown for Cox by ULorraine that the local calcite content plays a role in the effectiveness of the self-sealing process, whatever the material orientation (parallel or perpendicular to the bedding). For this clay, when carbonate content increases, the capacity of self-sealing decreases. This has been highlighted also by GRS but this set of experiments showed also that if a fracture network is distributed through both carbonate-rich and clay-rich regions, the self-sealing performance of the entire network is determined mainly by the clay-rich part of the network.

Contradictory results were obtained on the effect of temperature for clay host rocks: ULorraine and UGrenoble working on artificial cracked (sawed) Callovo-Oxfordian samples showed that temperature may have a delaying effect, but the final permeabilities are similar to those of samples tested at room temperatures and the scans show that the cracks are rapidly closed. On the other hand, the self-sealing experiments performed by BGS on sheared samples indicate that the self-sealing potential (SSP) becomes negligible at high temperatures in both the Opalinus Clay and the Callovo-Oxfordian claystone. Further analysis are needed to understand the processes inducing this behaviour or whether the SSP parameters are reliable indicators of the self-sealing efficiency.

Gas breakthrough through clay host rock can lead to dilatant pathways creation. Several experiments conducted during the project showed that the gas injection have a negligeable effect on the water permeability of the material. This has been highlighted on tests performed before and after gas injection by EPFL on Opalinus Clay or by UPC/CIMNE on Boom clay.

The self-sealing ability of bentonite is also essential for the safe design of a deep geological repository. Under high gas pressure loading, a dilatant pathway is formed in the bentonite, which may be a preferential pathway for radionuclide leakage. The GAS experiments on BCV bentonite showed that after three months of saturation following a breakthrough event, the sealing properties of bentonite are not compromised by breakthroughs caused by high gas pressure in key parameters (hydraulic conductivity and swelling pressure). No significant changes were also observed after one year of cyclic loading with fast gas tests. The conclusion that there is no effect on the sealing properties of BCV bentonite after repeated breakthrough events is the same for samples compacted homogeneously or with an artificial joint.

The project confirmed that modelling self-sealing processes in host rock is a real challenge. Few models are available or have been developed to model self-sealing processes in the clay host rock. The work performed by ULG integrating in the LAGAMINE code a new hydro-mechanical constitutive model based on several experimental observations gives interesting results. This model is based on the observation that the saturation phase generates micro-cracks around the fracture, defining a low-density and fairly compressible zone. It was able to reproduce experimental tests performed on fracture samples. Both the fracture closure during hydration and the fracture opening when the fracture material is submitted to drying are well reproduced.

Overall, these results are very promising and give confidence in the self-sealing capacity of both the bentonite barriers and of the clay rocks identified to host radioactive waste disposals.

References

Ammen, M., Palten, P.-J. (2021). TBO Trüllikon-1-1: Drilling. Nagra, NAB 20 09.

Auvray, C., Grgic, D., Morlot, C., Fourreau, E., & Talandier, J. (2015). X-Ray Tomography Applied to Self-Healing Experiments on Argillites. 13th ISRM International Congress of Rock Mechanics, Montréal, (Québec, Canada)

Bastiaens W., Bernier F., Li X.L., (2007). SELFRAC: Experiments and conclusions on fracturing, self-healing and self-sealing processes in clays, Physics and Chemistry of the Earth, Parts A/B/C, Volume 32, Issues 8–14, Pages 600-615, https://doi.org/10.1016/j.pce.2006.04.026.

Bernier F., Li X.L. et al, (2007). Fractures and Self-healing within the Excavation Disturbed Zone in Clays (SELFRAC) - Final report. European Commission Report, EUR 22585. https://cordis.europa.eu/docs/projects/files/FIKW/FIKW-CT-2001-00182/selfrac_projrep_en.pdf

Bock, H. et al., (2010). Self-sealing of Fractures in Argillaceous Formations in the Context of Geological Disposal of Radioactive Waste. https://www.oecd-nea.org/rwm/reports/2010/nea6184-self-sealing.pdf

Cerfontaine B., Dieudonné A.-C., Radu J.-P., Collin F., Charlier R. (2015). 3D zero-thickness coupled interface finite element: formulation and application. Comput Geotech 69:124–140. https://doi.org/10.1016/j.compgeo.2015.04.016

Charlier R. (1987). Approche unifiée de quelques problèmes non linéaires de mécanique des milieux continus par la méthode des éléments finis: (grandes déformations des métaux et des sols, contact unilatéral de solides, conduction thermique et écoulements en milieu poreux)

Collin F. (2003). Couplages thermo-hydro-mécaniques dans les sols et les roches tendres partiellement saturés

De Craen M., Wang L., Van Geet M., Moors H. (2004). Geochemistry of Boom Clay pore water at the Mol site, SCK-CEN-BL-990 04/MDC/P-48, SCK-CEN

Di Donna A., Charrier P., Dijkstra J., Andò E., Bésuelle P. (2022). The contribution of swelling to self-sealing of claystone studied through x-ray tomography, Physics and Chemistry of the Earth, Parts A/B/C, 127, 103191, https://doi:10.1016/j.pce.2022.103191

Ferrari, A. and Laloui, L. (2013). Advances in the testing of the hydro-mechanical behaviour of shales. In: Multiphysical Testing of Soils and Shales, Springer: 57-68.

Ferrari, A., Favero, V. and Laloui, L. (2016). One-dimensional compression and consolidation of shales. International Journal of Rock Mechanics and Mining Sciences 88: 286-300.

Giot, R., Auvray, C., & Talandier, J. (2019). Self-sealing of claystone under X-ray nanotomography. Geological Society, London, Special Publications, 482(1), 213–223. https://doi.org/10.1144/SP482.4

Gonzalez-Blanco, L., Romero, E. & Levasseur, S. (2023). Self-Sealing of Boom Clay After Gas Transport. Rock Mechanics and Rock Engineering. Available at: https://doi.org/10.1007/s00603-023-03529-3

Gonzalez-Blanco, L., Romero, E., Jommi, C., Li, X., & Sillen, X. (2016). Gas migration in a Cenozoic clay: Experimental results and numerical modelling. Geomechanics for Energy and the Environment, 6, pp.81–100. http://linkinghub.elsevier.com/retrieve/pii/S2352380816300260.

Gonzalez-Blanco, L., Romero, E. & Levasseur, S. (2023). Self-Sealing of Boom Clay After Gas Transport. Rock Mechanics and Rock Engineering. https://doi.org/10.1007/s00603-023-03529-3

Gonzalez-Blanco, L., Romero, E., Marschall, P., & Levasseur, S. (2022). Hydro-mechanical Response to Gas Transfer of Deep Argillaceous Host Rocks for Radioactive Waste Disposal. Rock Mechanics and Rock Engineering, 55(3), pp.1159–1177. https://doi.org/10.1007/s00603-021-02717-3

Code de champ modifié

Code de champ modifié

Gonzalez-Blanco, L. & Romero, E. (2024). A multi-scale insight into gas migration in a deep Cenozoic clay. Géotechnique 74, No. 4, 337–354. https://doi.org/10.1680/jgeot.21.00208

Grgic, D., Bésuelle, P. & Cuss, R. (2023). Technical report on thermal effects on near field properties. Final version as of 01.11.2023 of deliverable D7.3 of the HORIZON 2020 project EURAD. EC Grant agreement no: 847593.

Levasseur et al, (2021) EURAD Deliverable D6.1 - Initial State of the Art on Gas Transport in Clayey Materials Report number: Deliverable D6.1 of the HORIZON 2020 project EURAD, Work Package Gas. EC Grant agreement no: 84759

Marschall P., Talandier J., Kolditz O., Kucerova M., Mokni N., Grgic D., Agboli D., Zhang C.-L., Cuss R., Wiseall A., Gonzalez-Blanco L., Romero E., Llabjani Q., Ferrari A. (2024). Deliverable D6.8 of the HORIZON 2020 project EURAD, Work Package Gas. EC Grant agreement no: 847593.

Roscoe K., Burland J.B. (1968). On the generalized stress-strain behaviour of “wet” clay. Engineering Plasticity (Papers for a conference held in Cambridge, Mar. 1968), Cambridge, University Press, 535–609.

Senger, R.K., Papafotiou, A., Marschall, P. (2014). Thermo-hydraulic simulations of the near-field of a SF/HLW repository during early- and late-time post-closure period. NAGRA Arbeitsbericht NAB 14-011.

Tsang, Ch.-F. and Bernier, F. (2005). Definitions of excavation disturbed zone and excavation damaged zone. –In: Davies, C. and Bernier, F. (eds.): Impact of the excavation disturbed or damaged zone (EDZ) on the performance of radioactive waste geological repositories, EUR 21028 EN: 5-8, Brussels (European Commission)

Villar, M.V. et al. (2023). D7.2 HITEC. Updated State-of-the-Art on THM behaviour of i) Buffer clay materials and of ii) Host clay formations. Deliverable D7.2 HITEC. EURAD Project, Horizon 2020 No 847593. 125 pp.

Wang C., Talandier J., Skoczylas F. (2022). Swelling and fluid transport of re-sealed Callovo–Oxfordian claystone. Rock Mech Rock Eng. https://doi.org/10.1007/s00603-021-02708-4

Zhang C.-L., Talandier J. (2023). Self-sealing of fractures in indurated claystones measured by water and gas flow. J Rock Mech Geotech Eng 15:227–238. https://doi.org/10.1016/j.jrmge.2022. 01.014

Code de champ modifié